1-1-2023

Molecular Dynamics Simulations for The Mechanical Behavior of Alpha Quartz with Void Defects Under Tension

Yu Jia
University of Mississippi

MOLECULAR DYNAMICS SIMULATIONS FOR THE MECHANICAL BEHAVIOR OF ALPHA QUARTZ WITH VOID DEFECTS UNDER TENSION

A Thesis
presented in partial fulfillment of requirements
for the degree of Master of Science
in the Department of Mechanical Engineering
The University of Mississippi

By

YU JIA

August 2023

ABSTRACT

The structural and mechanical properties of void-free and single-void α-quartz were investigated using MD simulations with three different interatomic potentials (BKS, Vashishta and Tersoff). Two distinct ensembles, NVT and NPT, were separately applied to investigate the tensile response of α-quartz under uniaxial strain and uniaxial stress states. A comprehensive comparison among different potentials, as well as comparison with currently available experiments, has been made. The BKS and Vashishta potentials accurately predicted the structural properties of void-free α-quartz, while the Tersoff potential was deviated significantly from the experimental data. Under tension, the BKS did a better description for the mechanical performance of α-quartz. The Vashishta potential also captured the tension behavior, but overpredicted the Young's modulus. The Tersoff potential accurately described the elastic deformation but was unable to predict the fracture behavior for α-quartz. Furthermore, the void-size effect on the tensile and fracture behavior of α-quartz was analyzed and the predictions by using all three potentials were compared. Additionally, the choice of the ensembles could influence the mechanical response of α-quartz. The presence of a small void with a radius of 2.5 Å, when using an NVT ensemble with the BKS potential, significantly affected the tensile properties, while the NPT simulation did not show the same effect. The tensile curves obtained by using the Vashishta potential were similar in both NVT and NPT simulations, with slightly higher tensile properties observed in the NPT simulation. With Tersoff potential, brittle fracture occurred at a strain of 0.33 in NVT simulation but was not observed in NPT simulation. The equivalent stress analysis reveals that the BKS potential can better describe the stress concentration around the voids, while the Vashishta and Tersoff

potentials cannot show satisfactory description on the material fracture with the presence of the voids. Based on all the above-mentioned comparisons, the BKS potential is demonstrated to be the most suitable one to describe α-quartz under tension. All the findings in this work highlight the importance of a proper selection of interatomic potentials for simulating the properties of nano-void structures, especially for the study of fracture mechanisms in silica materials.

DEDICATION

To my family.

LIST OF ABBREVIATIONS AND SYMBOLS

Acronyms

MD	Molecular dynamics
BKS	Potential developed by van Beest, Kramer and van Santen
LRL	Lawrence Radiation Laboratory
NVE	Ensemble with fixed number of particles, volume and total energy in the system
NVT	Ensemble with fixed number of particles, volume and temperature in the system
NPT	Ensemble with fixed number of particles, pressure and temperature in the system
PBC	Periodic boundary condition
LAMMPS	Large-scale Atomic Molecular Massively Parallel Simulator
MPI	Message Passing Interface
OVITO	Visualization and analysis software for molecular simulation
GUI	Graphical user interface
GCCM	Generalized crystal-cutting method

Roman symbols

Fi	Force
m_i	Mass
$\boldsymbol{a}_i$	Acceleration
T	Temperature
P	Pressure
N	Number of particles
V	Volume
E	Total energy
r_{ij}	Distance between atoms
Q	Fixed charge
A_{ij}	BKS parameter
B_{ij}	BKS parameter
C_{ij}	BKS parameter
H_{ij}	Strength of the steric repulsion
W_{ij}	Strength of the van der Waals interaction
D_{ij}	Charge-dipole interaction
Z_i	Effective charge
f_{ij}^{A}	Attractive pair potential
f_{ij}^{R}	Repulsive pair potential
f_{ij}^{C}	Cut-off function
R	Cut-off distance

Greek symbols

ϕ_{ij}	Total potential energy
η_{ij}	Exponent of the steric repulsion
ξ	Length of the charge-dipole
λ	Length of Coulomb interaction
σ	Stress
ε	Strain
σ_{VM}	Von Mises stress
ε_f	Fracture strain

ACKNOWLEDGMENTS

First and foremost, I wish to thank my advisor, Prof. Shan Jiang, a source of inspiration and guidance throughout the process. Although there were many difficult times during my research, he always encourages me and keeps my study in the right direction. I am also grateful for the financial support that Prof. Shan Jiang has offered me to work on this project.

I would like to gratefully thank Prof. Arunachalam Rajendran and Prof. Yiwei Han for serving on my examination committee for my master thesis and providing scientific guidance along the way. I would also like to express my gratitude towards the Department of Mechanical Engineering, as well as School of Engineering at Ole Miss. The faculty and administrative staff members are extremely helpful and friendly.

I express my sincere thanks to Prof. Shan Jiang's group members: Huadian Zhang (Ph.D. Candidate) and Qingrui Jiang (Ph.D. Candidate) for their insightful thoughts and suggestions while doing my study and research.

Last but not least, I would like to thank my family for their unconditional support.

TABLE OF CONTENTS

LIST OF TABLES

LIST OF FIGURES

CHAPTER 1

INTRODUCTION

1.1 Introduction to silica and quartz

Silica dioxide, also known as silica, is an oxide of silicon with the chemical formula of SiO_2. It is the most abundant oxide found in the earth's crust [1]. More than 90% of the crust's volume is comprised of silicate minerals, composed of silica and various other molecules [2]. They are also primary components of the crusts of the Moon, Mercury, Venus, and Mars [3]. Silica has various applications due to its unique properties in different fields. It is the primary raw material in the production of glass and ceramics, and in the electronics industry, silica plays a vital role as it is utilized to produce silicon for computer chips. Moreover, the majority of fiber optic cables for telecommunications are also made from silica. Silica has been largely used in construction industry as well, e.g. for the production of concrete, and it has been found applications beyond these industries too. It serves as a soil additive to improve plant growth in agriculture. Additionally, it is a common additive in food and cosmetics production. Silica's versatility extends further as it is employed as a desiccant to absorb moisture and as a filler in rubber and plastics. Given its broad range of applications, silica is extensively studied and researched in various fields. Its significance in numerous industries, coupled with its abundant presence, makes it an intriguing material for scientific exploration.

Silica is found in various forms with their unique properties and uses. The most common types of silica are cristobalite, tridymite and quartz. Cristobalite and tridymite are polymorphs of SiO_2 in which the silica tetrahedra are packed in a two-layer structure (tridymite) or a three-layer structure (cristobalite). Cristobalite is a dominant mineral found in volcanic rocks and can also be observed as a detrital mineral in soils formed from pyroclastic volcanic materials. However, it is rare in other soil types. Cristobalite is used in some applications, such as refractory materials, fillers in polymers and polishing abrasives. Tridymite is found in various volcanic materials such

as trachybasalt and tuffs, as well as in limestone. It could be used in the production of ceramics and refractory materials.

Quartz is the most abundant form of silica and has been widely used in various industrial applications due to its great economic importance. Among all the varieties for quartz, α-quartz and β-quartz are two of the most common polymorphs. Alpha-quartz (or low quartz) is stable at the room temperature and pressure, while beta-quartz (or high quartz) is thermodynamically stable at temperatures above 573 °C. As the temperature increases to around 573 ℃, α-quartz will transform into β-quartz, and this transformation process is spontaneous and reversible. Both of them have been extensively studied in various areas, such as chemistry, mechanics, biophysics, geoscience and electronics [4–6].

1.2 Porous or void-containing materials

Porous or void-containing materials with pore/void sizes ranging from molecular to micrometer have interesting mechanical and thermal properties that make them suitable for many science and/or engineering applications [7]. J. S. Beck et al. first reported the porous silica, and since then, numerous porous materials with varying pore sizes, pH levels (ranging from highly basic to strongly acidic conditions), and shapes have been synthesized using non-ionic, cationic, neutral, and anionic surfactants [8–12]. These materials exhibit desirable properties such as high surface area, uniform pore structures, and narrow pore size distributions. Those porous materials with their large pore volumes have demonstrated potentials in loading guest species and accommodating expansion and strain relaxation during repeated electrochemical energy storage processes. Furthermore, their high surface areas offer numerous reaction and interaction sites for various

surface processes, including catalysis, adsorption, energy storage, and separation. These features make them particularly well-suited for applications in energy conversion and storage [13–15].

When porosity, pore size/shape, and pore distribution in these materials are tailored, they can be used for thermal insulation, drug delivery, and microelectronics applications among others [16–20]. Pores, voids, and vacancies may sometimes be introduced to the structure of virgin materials during long-term use. For example, optical fibers made from quartz contain radiation-induced vacancies, which could significantly reduce the mechanical strength of the fibers during long-term operation. In general, the presence of pores or voids alters the crystalline structure of the material, thereby either complicating its physico-mechanical behavior or accelerating defect propagation and, hence, fundamentally deteriorating its overall performance [21]. These effects are more pronounced for complex multi-physics scenarios.

1.3 Literature review

The origin of the simulation of the properties of silica dates back to the 1980s [22], soon after the development of computer modeling. Over the last decades, advancements in computational methods have enabled the scientists and engineers to better predict the bulk and surface properties of different materials, including crystalline quartz. Among the widely used computational methods is molecular dynamics (MD) simulation, which is a useful tool for investigating the molecular-scale phenomena behind the evolution of microstructures and observed physico-mechanical properties of materials. Through an atomistic level description, MD simulation enables the analysis of nanostructure evolution on the nanoseconds time scale for systems that comprise of millions and sometimes billions of atoms. Moreover, by probing the time evolution of the interactions between the constituent atoms of the material, its dynamic, thermodynamic, and mechanical

properties can be estimated. This is possible through the use of a suitable interatomic potential or force field. Historically, Alder and Wainwright, two pioneers of MD simulation, studied the interactions of hard spheres in late 1950s [23,24]. However, it was not until 1964 that the first interatomic potential, which was used by Rahman [25], yielded realistic predictions of the properties of argon. Since then, many interatomic potentials have been developed. Given the fact that the accuracy of material property predictions depends on the reliability and transferability of the interatomic potential used for a given simulation, it is pivotal to first evaluate the potential in terms of its capability in reproducing some target material properties.

Based on the thermodynamic and mechanical parameters of temperature, pressure, and strain rate, α-quartz can undergo either brittle or ductile failure under an external load. The tension behavior of α-quartz has been simulated in past decades using different interatomic potentials [22,26–36]. The timeline of these simulations is provided in Figure 1, where each simulation work is designated by the name of the first author of the corresponding publication. For example, Molaei et al. investigated the mechanical properties and crack propagation mechanism of α-quartz through a series of MD simulations using the van Beest, Kramer, and van Santen (BKS) pairwise interatomic potential [5] and Tersoff potential [37] separately in their study. They determined the stress-strain behavior of α-quartz under uniaxial tensile loading at different temperatures and strain rates, and successfully correlated between them. Chowdhury et al. [28] predicted the crystalline-to-amorphous transition of silica during tension using the reactive force field (ReaxFF). The quasi-static modulus, which was calculated from a power-law fitting to the low-strain-rate data obtained by ReaxFF simulation, is in good agreement with the experimental data. The effects of strain rate, as well as heating and cooling rates, on the nanostructure of silica and its stress-strain response were also investigated. In another work, Wang et al. [26] determined the tensile behavior of

amorphous silica through MD simulation with the Tersoff potential. The transition of deformation from elastic to plastic at different strain rates was correctly captured in their work.

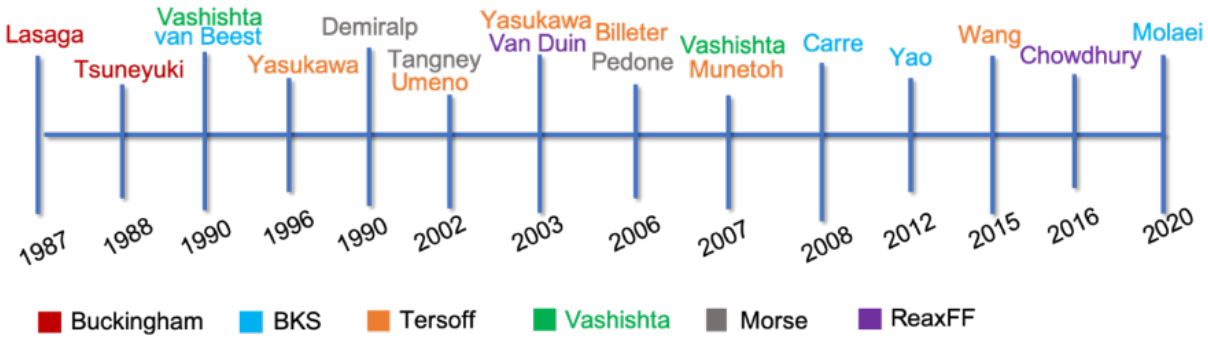

Figure 1. Timeline showing the development of interatomic potentials for α-quartz.

Previously, some theoretical and computational investigations of the porous structure of α-quartz and its mechanical properties under load were attempted by researchers to provide insights into the experimentally observed failure mechanisms and to aid the experimental efforts. For example, Molaei [37] found that the central cracks in α-quartz decreased the average stress and strain, and this reduction was much higher in the z-direction ([0 0 1]). In general, porosity, which is defined as the void-to-total-volume fraction, is usually used as a principal characteristic of the porous material when deriving correlations between its void structure and continuum behavior [38–40], with the consideration of void size and shape often ignored. One of the reasons for only considering porosity is that quantifying the micro-void structure at continuum level is a challenging task.

1.4 Structure of the thesis

While these published results provide confidence in using MD simulation to predict the mechanical properties of α-quartz, the fact that many different interatomic potentials were used to make the predictions merits a closer scrutiny of these potentials. This is especially true for an α-quartz single crystal structure with void defects, where different potentials may deviate in their predictions of the mechanical and fracture behavior of the material. Herein, three widely used interatomic potentials for α-quartz, i.e., BKS, Vashishta, and Tersoff were used to determine the physical and mechanical properties of defect-free and single-void α-quartz with two different void sizes. The remaining part of the thesis is organized as follows. In Chapter 2, details on the computational approach, including MD simulations, and theoretical background on interatomic potentials are provided. Then in Chapter 3 presents the modelling and simulation processes for both void-free and single-void α-quartz models. In Chapter 4, the results for structural and mechanical properties of α-quartz are presented by utilizing three different potentials and, finally, conclusions from the previous chapters are summarized in Chapter 5, together with suggested future work.

CHAPTER 2

MOLECULAR DYNAMICS METHODOLOGY

2.1 Introduction

By capturing the motions of atoms and their interactions, computer simulations have become a valuable tool for investigating the dynamics of material systems. This has enabled researchers to explore specific questions about the properties and functions of various materials systems. Conventional MD simulation is one of the most frequently employed computational techniques for examining equilibrium and transport properties in many-particle systems. It is a computational technique used to study the motion and interactions of atoms and molecules over time and it involves solving the equations of motion for a system of interacting particles, usually in the context of classical mechanics.

MD simulations were first proposed in the 1950s by Alder and Wainwright [23,41] at the Lawrence Radiation Laboratory (LRL) in the United States. They used the then available highly powerful mainframe computers at LRL to calculate the response of several hundred interacting classical particles in the fields of equilibrium and non-equilibrium statistical mechanics. Since then, MD simulation has been extensively used in various fields such as crystal growth, indentation, tribology, fracture, and laser interactions, among others [42–46]. This has led to numerous publications and several books on the topic, making MD simulation a matured field [42,47,48].

The fundamental principle behind MD simulations is to simulate the behavior of a system by numerically integrating the equations of motion for all the particles in the system. MD simulations involve numerically integrating the equations of motion for all particles in a system to simulate its behavior. The method relies on solving Newton's equations of motion for an atom ensemble via numerical techniques over short time intervals, and computing equilibrium statistical averages as temporal averages. To accurately describe interatomic forces, explicit knowledge of the electronic ground state in each system configuration is required. However, to make atomistic

simulation studies practical, a classical or semi-classical potential that meets material properties criteria, including lattice constant, energy of sublimation, compressibility, elastic constants, the equation of state, and the crystal's stability, is used to derive interatomic forces.

MD simulations utilize a potential energy function to calculate the forces acting on each particle in a system, considering both bonded and non-bonded interactions, such as van der Waals and electrostatic forces. This simulation method can be likened to analyzing the dynamic response of nonlinear spring-mass systems under various conditions. From this point of view, MD simulation is similar to other analyses that mechanical engineers routinely conduct, such as the investigation of vibrations of a mechanical system wherein a series of springless masses and massless springs are connected and the response of the system is investigated under a given external load.

MD simulation is particularly useful for studying the statistical properties of condensed matter systems at an atomistic level, providing valuable information that is not easily obtainable through other theoretical methods or experiments. Recent advancements in computational speed and memory storage have made it possible to study a range of phenomena in materials science, including the introduction of defect structures and the analysis of simple nanostructured materials. This computational method has contributed to a deeper understanding of the properties of materials, drug design, biological membranes, and the behavior of fluids and phase transitions in physics. It has become a critical tool for scientists to seek a better understanding for complex microscale systems and has played a crucial role in advancing our knowledge of the natural world.

2.2 Molecular Dynamics Simulations

2.2.1 Basic Idea of Molecular Dynamics

The MD simulations are based on Newton's laws of motion, which describe the behavior of particles in a classical mechanics system. Using this method, most notably the Newtonian formalism:

$$F_i = m_i \boldsymbol{a}_i \quad (1)$$

are followed for each atom i in the system has a mass m_i, an acceleration $\boldsymbol{a}_i$ given by $d^2\mathrm{r_i}/dt^2$, and experiences a force Fi due to interactions with other atoms. The forces acting on the atoms are typically obtained from classical interatomic potentials or from quantum mechanical ab initio calculations. The thermodynamic state of a system is characterized by a few key parameters: temperature (T), pressure (P), and the number of particles (N). The microscopic state of the system, on the other hand, is described by the positions and velocities of the individual atoms, which exist in a multi-dimensional phase space. In a system consisting of N particles, the phase space has 6N dimensions. An Ensemble refers to a collection of points in phase space that satisfy the conditions of a particular thermodynamic state. In MD simulations, a sequence of points in phase space is generated over time, representing different conformations of the system that belong to the same ensemble.

2.2.1 Ensembles

A thermodynamic ensemble provides a way to derive the thermodynamic properties of a system through the laws of classical and quantum mechanics. The main idea is that different ensembles represent systems with different degrees of separation from the surrounding environment, ranging from completely isolated systems (i.e., microcanonical ensemble) to completely open ones (i.e., grand canonical ensemble). The choose of ensemble depends on the

specific problems and the conditions for the simulation. There are three primary ensembles used in MD simulations: NVE, NVT and NPT ensembles.

NVE Ensemble is a statistical ensemble that is used to describe a closed system that is isolated from its surroundings. In the NVE ensemble, the number of particles (N), volume (V) and total energy (E) of the system are fixed, therefore, corresponds to an isolated system that cannot exchange heat or matter with the outer environment. By employing the NVE ensemble, the result is a system where the total energy is conserved but fluctuations in potential and kinetic energy are still allowed. For the NVT ensemble, N, V and T are fixed, which means the system is allowed to exchange heat with outer space so that the temperature stays constant. of the system are fixed, but the system is allowed to exchange energy with its surroundings while maintaining a constant temperature (T). The NVT ensemble is particularly useful for studying systems that are in contact with a heat bath, where energy can be exchanged with the surroundings to maintain a constant temperature. For the NPT ensemble, N, P and T are fixed during each time step, so it means that the total energy and volume of the system are not conserved, but the system's macroscopic properties such as temperature, pressure, and density are determined by both the system's internal energy, volume, and the energy and volume exchange with the surroundings.

In addition to these primary ensembles, other ensembles, such as the Gibbs ensemble and the isobaric-isothermal ensemble, may also be used in specific cases. The choice of ensemble depends on the specific physical conditions of the system being studied and the properties being simulated. In this work, two different ensembles, NVT (constant Number of particles, Volume, and Temperature) and NPT (constant Number of particles, Pressure, and Temperature), were separately applied to investigate the uniaxial strain and uniaxial stress behaviors of α-quartz.

2.2.2 Boundary Conditions

Boundary conditions in molecular dynamics simulations specify how a simulated system interacts with its environment or boundary. They play a critical role in determining the behavior of the system under study. For simulation purposes, a designer needs to set the boundary conditions in their simulation to determine a steady state solution to the differential equation they are investigating. There are two main types of boundary conditions we used in our simulations: periodic boundary conditions and fixed boundary conditions. In periodic boundary conditions (PBC), a set of boundary conditions which are chosen for approximating a large system by using a small part called a unit cell. The system is replicated infinitely in all directions, and the periodic images of the original system are treated as if they are identical copies of the original system. PBC are usually applied to calculate bulk gasses, liquids, crystals, or mixtures. A common application uses PBC to simulate solvated macromolecules in a bath of explicit solvent. In fixed boundary conditions, the system is placed in a finite box, and the atoms in the system interact with the walls of the box. Those boundaries are both rigid enough to maintain the structure and flexible enough to interact with other atoms. This approach is used to simulate systems that have a well-defined boundary, such as a molecule in solution or a protein in a membrane. The choice of boundary conditions depends on the system under study and the scientific question being addressed. Each type of boundary condition has its own advantages and limitations, and researchers must carefully choose the appropriate boundary conditions to ensure that the simulation accurately represents the real system being studied. In my work, PBC is used in all MD simulations.

2.2.3 Minimization

In MD simulations, energy minimization is essential to determining the proper atomic arrangement due to the unfavorable energetic nature of drawn chemical structures. The potential energy of an atomic structure comprises various components, such as stretching, bending and torsion. Consequently, when employing an energy minimization program, it rapidly converges to a local minimum energy value. Minimization is typically performed as a preprocessing step before running an MD simulation, as it can help to ensure that the starting configuration of the system is reasonable.

There are several different algorithms could be used for minimization, such as steepest descent, conjugate gradient, and quasi-Newton methods. Steepest descent method is a simple and widely used method that iteratively adjusts the position of each atom along the steepest descent direction of the potential energy surface until a minimum is found. Conjugate gradient method is an improvement over the steepest descent method and considers the previous search direction. It uses conjugate directions to minimize the energy and is often more efficient than the steepest descent method. Quasi-newton method is another algorithm to use an approximation of the Hessian matrix to estimate the curvature of the potential energy surface and determine the search direction. These algorithms differ in their efficiency and accuracy, and the choice of method will depend on the size and complexity of the system being studied. In my work, I used conjugate gradient schemes for the minimization prior to conducting MD simulations.

2.3 Software Packages

2.3.1 LAMMPS molecular dynamics simulator

The MD simulations in this thesis were performed using the Large-scale Atomic Molecular Massively Parallel Simulator (LAMMPS) which is a widely used software package written in C++. It was developed at Sandia National Laboratories and is distributed as an open-source code [49].

LAMMPS is designed to simulate a variety of material systems, including solids, liquids, and biomolecules. It can handle a wide range of interatomic potentials and force fields, and supports various ensemble methods, such as NVT, NPT, and NVE, for performing MD simulations under different thermodynamic conditions. LAMMPS is also highly scalable and can efficiently run on parallel computing architectures, such as clusters and supercomputers to allow simulations of large structures with millions or billions of atoms. It provides a flexible and extensible framework for users to implement their own custom algorithms and models. This software is obtained as source code and can be compiled on a variety of computer architectures with optional packages that may be useful to specific applications. To optimize performance, LAMMPS is implemented using the MPI (Message Passing Interface) message passing library for parallel processing. In this case, LAMMPS uses spatial decomposition techniques to partition the simulation region into smaller sub-domains each assigned to a different processor. All the processes communicate results and atom information is stored for atoms that border the sub-domains. In our simulations, multicore processors were used to take advantage of the parallel processing capabilities of LAMMPS.

The input script for LAMMPS begins by specifying the type of units to be used for thermodynamic activity, such as real or atomic. The atom_style command determines the attributes associated with the atoms and must be used prior to setting up a simulation using the read_data command. The simulation setup requires establishing the boundary conditions, which can be accomplished using styles p, f, s, or m. In our simulation, style p was used, indicating that the box

is periodic and that particles interact with their mirrored images across the boundary. The coordinates of atoms in the substrate can be read from an external file or generated within the LAMMPS input script by creating a lattice, assigning groups to atoms, and creating atoms.

The main part of the input script is the problem settings. The potentials to be used in the simulation are referenced using the pair_style and pair_coeff commands. The parameter group is used to limit the MD integration to a specific group of atoms, which can be named by the user using the appropriate symbol. Additionally, the time for each step in the simulation, thermodynamic fixes, and commands for storing the coordinates and results of the simulation in a log file must be specified. In our simulations for α-quartz, a timestep of 1.0 fs was used.

2.3.2 Visualization

OVITO is a visualization and analysis software for atomistic and particle-based simulations in materials science, chemistry, and related fields. It provides a graphical user interface (GUI) for visualizing, analyzing, and manipulating large datasets of atomic configurations produced by molecular dynamics (MD) simulations, Monte Carlo simulations, or other particle-based simulations.

OVITO supports a wide range of file formats commonly used in atomistic simulation, including LAMMPS, GROMACS, VASP, and many others. It allows users to visualize the atomic structure of a simulation system in three dimensions, generate snapshots of the system at different time steps, create animations, and analyze properties of the simulation output, such as the distribution of particles, the bond lengths, angles and dihedrals, and the energy landscape of the system.

In addition to its powerful visualization capabilities, OVITO also provides a Python scripting interface that allows users to automate and customize their analysis workflows. With this interface, users can access the underlying data structures and algorithms used by OVITO and perform complex analyses or custom calculations on the simulation data.

2.4 Interatomic potentials

In MD simulations, interatomic potentials are a set of mathematical functions to describe the interactions between particles (atoms, molecules, ions, etc.) in a system. The potential functions, also called the force fields, are defined in terms of a set of parameters that determine the strength and shape of the particle interactions. They provide a way to calculate the total energy of the system as a function of the positions and velocities of all the particles. Moreover, the forces acting on each particle at each time step can be determined using the same potential function, which in turn affects the movement of the particles according to Newton's laws of motion. Both bonded and non-bonded interactions would be represented using analytical functions, look-up tables, or more complex algorithms. The choice of potential function is critical in MD simulations as it determines the accuracy of the simulation results. The potential function must be able to reproduce the experimental or theoretical data for the system being studied and must also be computationally efficient to allow for large-scale simulations.

2.4.1 BKS Potential

The BKS potential was proposed by van Beest, Kramer, and van Santen in 1990 [32]. It is a two-body potential model which is composed of three major force field terms the nonbonded repulsion, the dispersive attraction, and the long-range electrostatic interactions. The parameters

for the repulsive and attractive terms are derived from iterative fitting to an ab initio potential energy surface of a H_4SiO_4 cluster and simultaneously optimizing the effective charges on the silicon and oxygen atoms to the bulk properties. The structural stability of the silica polymorphs is largely governed by an interplay of the electrostatic and the short-range atom-atom repulsive forces. Specifically, the total potential energy (ϕ_{ij}) is determined by:

$$\phi_{ij}(r_{ij}) = \frac{Q_i Q_j}{r_{ij}} + A_{ij} e^{-B_{ij} r_{ij}} - \frac{C_{ij}}{r_{ij}^6} \quad (2)$$

where i, and j represent atom species (e.g., Si or O) with a distance of r_{ij}. The A_{ij}, B_{ij}, and C_{ij} are BKS parameters that are listed in Table 1 [50]. Fixed charges are assigned to the atoms with the values Q_{Si} = 2.4 and Q_O = −1.2. The form of BKS potential is the usual Buckingham form, with the addition of a Coulomb force term. The parameters A, B, and C in the Buckingham interaction [31,32] were optimized for different pairs of atoms using Hartree-Fock ab-initio calculations and experimentally-determined properties, including the elastic constants of α-quartz. The reason to choose a value of zero for the Si-Si interaction is the fact that only Coulombic interactions are considered for this pair. The Si–O bond is partially covalent and partially ionic. The BKS has been successfully applied to a wide range of molecular simulations, and its performance has been evaluated through the calculation of the static and dynamical properties of several polymorphs of SiO_2 using molecular dynamics methods. The pressure-volume equations of state for α-quartz, cristobalite [51], and stishovite [52,53], the pressure-induced amorphization transformation in α-quartz and thermally induced the α-β transformation in cristobalite could be well reproduced by this model [54].

Table 1. The BKS parameters involving crystalline and vitreous silica

	A (eV)	B (Å^{-1})	C (eV. Å^{6})
O – O	1388.7730	2.76000	175.0000
Si – O	18003.7572	4.87318	133.5381
Si – Si	0	0	0

2.4.2 Vashishta Potential

The Vashishta potential applied in this thesis is developed by Nakano et al. in 1994 [55], and it is an optimized form of 1990-version of the potential [56]. The applied interatomic potential is different from 1990-version one in that the long-range Coulomb interaction in the latter is replaced by the suitably adjusted Coulomb form. This potential comprises two-body and three-body covalent interactions, has been used successfully for molten, crystalline and amorphous states of normal SiO_2 and also permanently densified amorphous SiO_2 [56–58]. This potential has been applied in molecular dynamics studies to investigate the structural and dynamical correlations of silica under various densities and temperatures.

The two-body contribution to the potential considers steric repulsion due to atomic sizes, Coulomb interactions resulting from charge transfer, and charge-dipole interactions to account for the large electronic polarizability of anions. The three-body covalent contributions consist of O-Si-O and Si-O-Si interactions, which depend on the angle and distance between Si and O atoms. The function combines the repulsive, screened charge-dipole, screened Coulombic, and dispersion interactions with bond angle energies and can be expressed as:

$$\phi_{ij} = \sum_{i<j} \phi_{ij}^{(2)}(r_{ij}) + \sum_{i,j<k} V_{jik}^{(3)}(r_{ij}, r_{ik}) \quad (3)$$

$$\phi_{ij}^{(2)}(r) = \frac{H_{ij}}{r^{\eta_{ij}}} + \frac{Z_i Z_j}{r} e^{-r/\lambda} - \frac{D^{ij}}{r^4} e^{-\frac{r}{\xi}} - \frac{W_{ij}}{r^6} \quad (4)$$

$$\phi_{ijk}^{(3)}(r_{ij}, r_{ik}) = B_{jik} \frac{[cos\theta_{ijk} - cos\theta_0]^2}{1 + C_{ijk}[cos\theta_{ijk} - cos\theta_0]^2} \times \exp\left(\frac{\gamma_{ij}}{\gamma_{ij} - \gamma_0}\right) \exp\left(\frac{\gamma_{ik}}{\gamma_{ik} - \gamma_0}\right) \quad (5)$$

Table 2. The Vashishta potential parameters for quartz from Nakano et al. [55]

A(eV)	λ(Å)	ζ(Å)	r_c(Å)	r_0(Å)	ξ(Å)
1.592	4.43	2.50	5.50	2.60	1.00
i	σ_i(Å)		$Z_i(e)$		α_i(Å^3)
Si	0.47		1.76		0.00
O	1.20		-0.88		2.40
i - j	η_{ij}				
Si - Si	11				
Si - O	9				
O - O	7				
$i - j - k$	B_{jik}(eV)	θ_{jik}			
O – Si - O	4.993	109.47			
Si – O -Si	19.972	141.00			

Eq. (3) includes both the two-body and three-body terms. In Eq. (4), H_{ij} and η_{ij} are the strength and exponent of the steric repulsion, respectively. W_{ij} and D_{ij} represent the strength of the van der Waals and charge-dipole interactions, respectively, and Z_i is the effective charge. ξ and λ represent the screening lengths of the charge-dipole and Coulomb interactions and $r = r_{ij}$ denotes the distance between atoms i and j. The three-body term is given by Eq. (5). Notice that only the

bond-bending terms of O-Si-O and Si-O-Si triplets are present for this three-body potential. The values of the parameters in Eq. (4) and (5) are listed in Table 2. Using this total potential function, lattice-structure calculations have shown that α-cristobalite and α-quartz have the lowest and almost degenerate energies, consistent with experiments. β-cristobalite, β-quartz, and keatite have higher energies than α-cristobalite and α-quartz. MD calculations using this potential function have correctly described the short- and intermediate-range order in molten and vitreous states [59].

2.4.3 Tersoff Potential

The Tersoff potential is a widely used empirical interatomic potential in molecular dynamics simulations to model the interactions between atoms. It was developed by John Tersoff in 1989 [60] and finds extensive application in the study of covalent materials such as semiconductors, ceramics, and carbon-based materials. The Tersoff potential considers three-body interactions between atoms, which are not included in traditional pairwise potentials. This makes it particularly useful for modeling complex materials where three or more atoms may be involved in the formation of chemical bonds. The Tersoff potential is based on a set of empirical parameters that are fit to experimental data and first-principles calculations. These parameters determine the strength and distance dependence of the atomic interactions and are specific to each material being studied. Applications of the Tersoff potential include the study of crystal growth, the mechanical properties of materials, and the behavior of materials under extreme conditions such as high temperatures and pressures. It has also been used to study the properties of nanoscale materials and to simulate chemical reactions at surfaces and interfaces.

The Tersoff potential is a bond order potential that, unlike a pair potential, modifies the bond strength based on the angles between the bond and all other bonds. It was developed to model

covalent systems and applied successfully to C, Si, and O elements. This potential includes radial two-body repulsive and attractive exponentials. The repulsive term is modified by a factor, which depends on the three-body terms, local environment, and atomic coordinates. For example, an atom with many neighbors forms weaker bonds than an atom with few neighbors. The three-body Tersoff potential was first calibrated for Si and later extended to the Si–O system based on the ab-initio calculations performed by Munetoh et al. [61]. It has since been successfully used to describe the interactions of amorphous SiO_2. The potential energy E of an atomic system is taken to be:

$$E = \sum_i E_i = \frac{1}{2}\sum_{i \neq j} V_{ij} \tag{6}$$

The analytic form for the pair potential, V_{ij}, of the Tersoff model is specified by the next functions:

$$V_{ij} = f_{ij}^{C}(a_{ij} f_{ij}^{R} - b_{ij} f_{ij}^{A}) \tag{7}$$

$$f_{ij}^{R} = Ae^{-\lambda_1 r_{ij}} \quad f_{ij}^{A} = Be^{-\lambda_2 r_{ij}} \tag{8}$$

$$f_{ij}^{C} = \begin{cases} 1, & r_{ij} < R_1 \\ \frac{1}{2} + \frac{1}{2}\cos\left(\pi \frac{r_{ij} - R_1}{R_2 - r_{ij}}\right), & R_1 < r_{ij} < R_2 \\ 0, & r_{ij} > R_2 \end{cases} \tag{9}$$

Those equations depict the distance between atoms like i and j by r_{ij}, with f_{ij}^{A} representing the attractive pair potential and f_{ij}^{R} representing the repulsive pair potential. The bond strength is denoted by λ. a_{ij} is a term that limits the range of the repulsive potential and b_{ij} is a measure for bond order. f_{ij}^{C} is the cut-off function that ensures that only nearest-neighbor interactions are

considered to reduce computational cost [33,62]. R_1 and R_2 are two cut-off distances to be employed in the cut-off function f_{ij}^{C}.

CHAPTER 3

MODELLING AND SIMULATION PROCESS

2.2. Models of void-free and single-void α-quartz

α-quartz is composed of a monoclinic unit cell with three Si atoms and six O atoms. It has translational symmetry in any crystal plane along unit vectors *a*, *b*, or *c*. To conveniently perform the mechanical tests along one prescribed longitudinal direction with preserved periodic boundaries in the other two lateral directions, the monoclinic α-quartz unit cell was converted to an orthorhombic unit cell by using the "generalized crystal-cutting method" (GCCM) [63,64] along the [001] direction, as shown in Figure 2. The blue spheres are silicon atoms, while the red spheres represent oxygen atoms in the schematic diagram of the α-quartz unit cell. Energy minimization was performed by adjusting the atom positions before building the supercell. Next, a 3D periodic supercell was built by replicating the converted orthorhombic unit cell geometry by repeat factors of 5 × 8 × 66 along the *x*, *y*, and *z* directions.

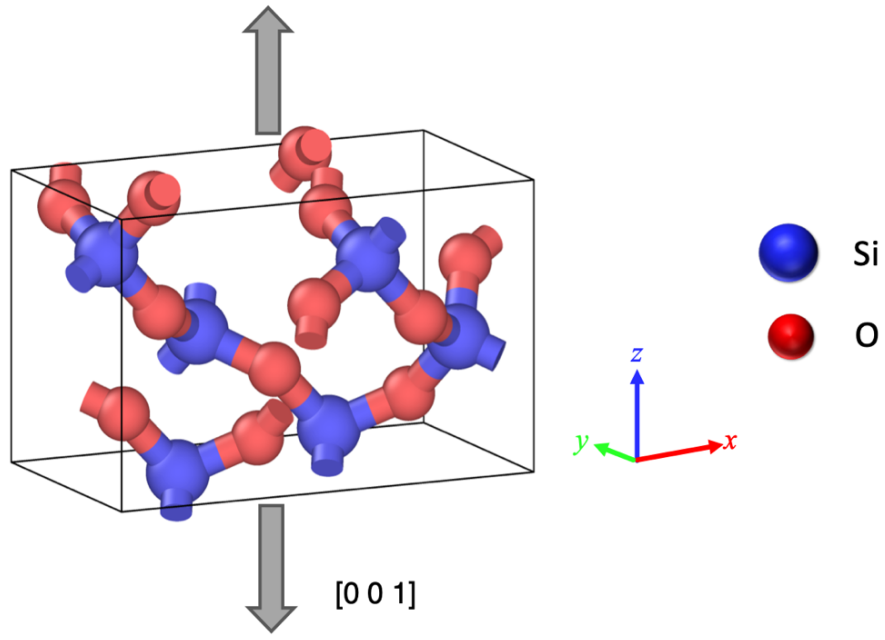

Figure 2. The unit cell of α-quartz after conversion from monoclinic to orthorhombic structure using the generalized crystal-cutting method with the tensile direction identified along the *z*-axis. The red spheres represent the oxygen atoms, while the blue spheres represent the silicon atoms)

Three crystalline α-quartz models with no void, small single-void (void radius = 2.5 Å), and large single-void (void radius = 15 Å) structures were generated (Figure 3a). The voids have spherical shape and are located in the middle of the single-void structures. The dimensions of the simulation box for all systems are around 42 Å×42 Å×320 Å. The void-free α-quartz system comprises 14,400 Si and 28,800 O atoms. The single-void models with the radii of 2.5 Å and 15 Å were generated by removing 6 and 1161 atoms from the void-free α-quartz structure, respectively. In Figures 3b and 3c, both the cross-sectional and front views of a portion of the supercells are provided for a better illustration of the void morphology in the single-void α-quartz structures.

2.3. Simulation procedure

MD simulations were performed using the three interatomic potentials introduced in Section 2.1, to assess their capability of reproducing the structural and material properties of void-free and single-void α-quartz structures. A time step of 0.001 ps was set for all simulations. For the initial structures, a Gaussian velocity distribution was applied to the entire systems, followed by a 100-ps equilibration simulation performed using an NPT ensemble (constant number of atoms, N; constant pressure, P; constant temperature, T) and 3D-periodic boundary conditions (PBC). This allowed the systems to be fully relaxed at 1 K and 1 atm. Next, the temperature was ramped from 1 K to 298 K and another 100-ps thermal equilibration was performed at 298 K. The tensile tests were then performed by stretching the structures along the z-direction at 298 K until failure.

Two different ensembles, NVT and NPT, were applied separately in the tensile tests to study the tensile properties in the uniaxial strain and uniaxial stress states for different α-quartz structures, respectively. The PBC for the case of NVT assures the uniaxial strain state during the

simulation process. However, for the NPT, in addition to the PBC, all stresses were enforced as zero except the axial stress to generate the uniaxial stress condition. The results were visualized and analyzed using the open-source OVITO visualization tool.

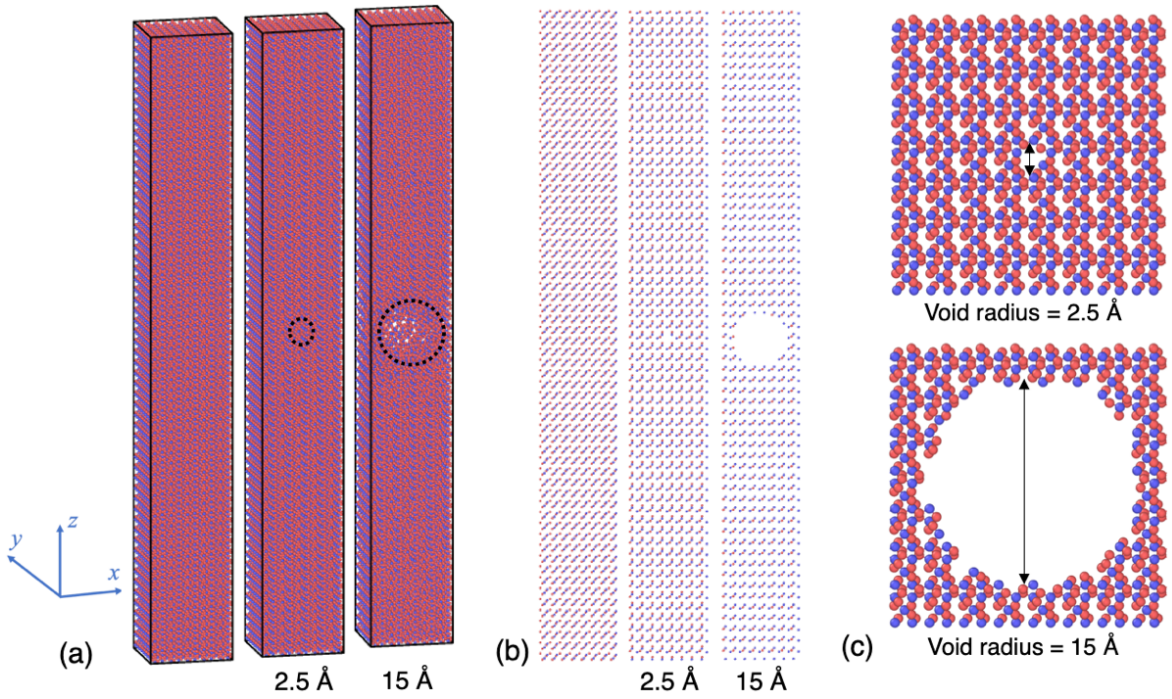

Figure 3. (a) Schematic views of the atomistic models for void-free and single-void α-quartz structures with two different void sizes of 2.5 and 15 Å; (b) Cross-sectional views of the α-quartz structures; (c) Front views of a portion of the microsopic structures of the single-void α-quartz structures.

CHAPTER 4

RESULTS AND DISCUSSION

3.1. Structural properties of α-quartz

In the tensile experiments and simulations, the structural properties and corresponding physical quantities are basically essential in determining the mechanical responses of the materials. The simulated structural properties of void-free α-quartz obtained using the BKS, Tersoff, and Vashishta potentials are compared with the experimental results in Table 3. The reported lattice constants and equilibrated densities were obtained based on the last 500 steps of the 500,000-step NPT equilibration simulations at 298 K. The density of α-quartz calculated using the BKS potential was 2.662 g/cm^3, which yields best agreement with the experimental value of 2.646 g/cm^3 reported by Cowen and El-Genk [65] among all the three potentials. The prediction made by Vashishta suggests a slightly lower density of 2.511 g/cm^3, which falls within an acceptable error range compared to the reported value. However, the Tersoff potential significantly underestimated the density of α-quartz.

Table 3. Predicted density and lattice parameters of perfect crystalline α-quartz by the BKS, Tersoff, and Vashishta potentials versus the experimental data.

	Density (g/cm^3)	***a* (Å)**	***b* (Å)**	***c* (Å)**
Exp. [65–67]	2.646	4.916	4.916	5.405
BKS	2.662	4.673	5.225	5.141
Tersoff	2.081	5.072	5.671	5.671
Vashishta	2.511	5.066	5.057	5.381

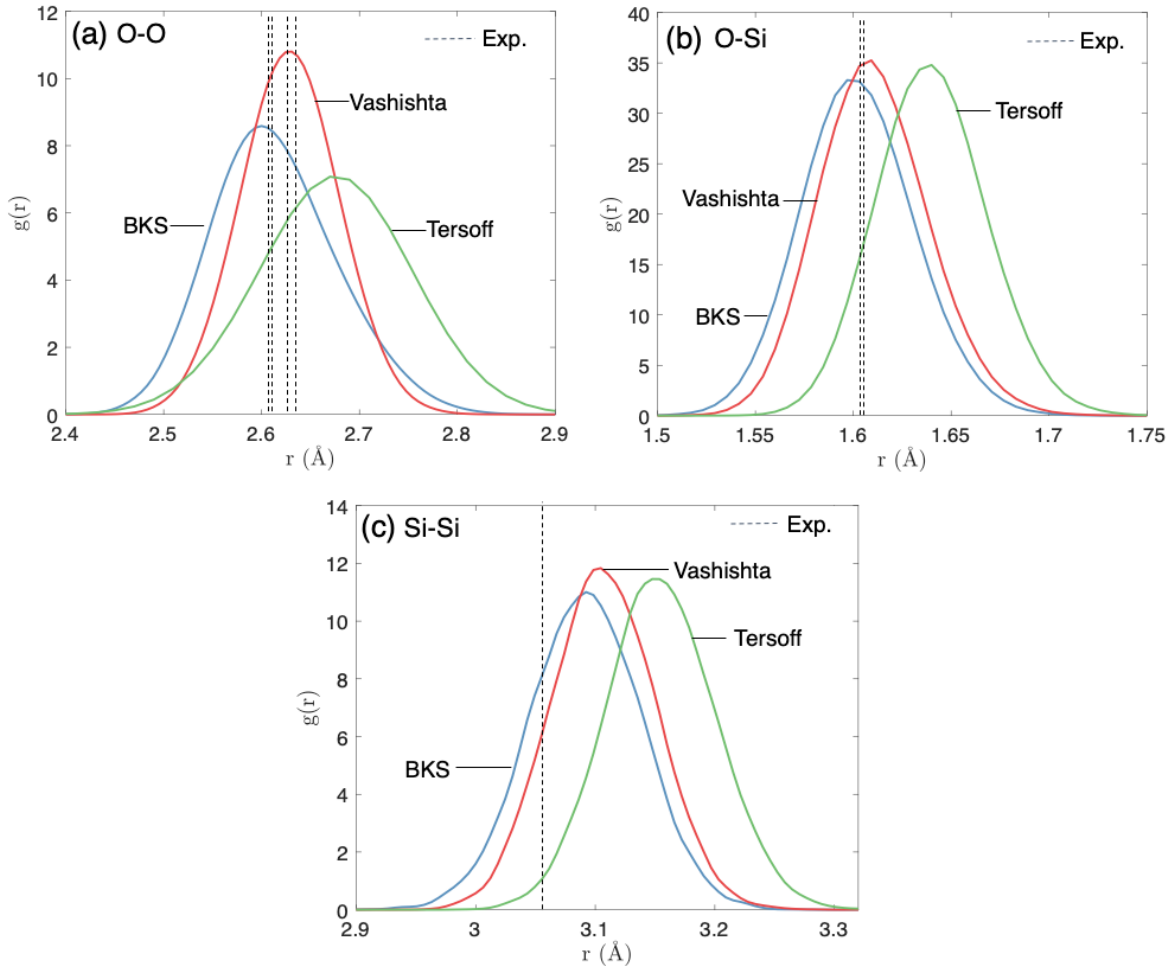

Figure 4. Radial distribution functions obtained for the (a) O-O, (b) O-Si, and (c) Si-Si bonds in void-free α-quartz at ambient conditions (298 K and 1 atm) using the BKS, Tersoff, and Vashishta potentials.

The lattice constants for the a, b, and c directions, calculated using the Vashishta potential, exhibited an excellent agreement with the experimental values, with a difference of only ~3%. Similarly, the lattice parameters predicted by the BKS potential show a good agreement as well, within ~5% of the experimental values. However, the Tersoff potential significantly deviated from the experimental values, especially for the lattice constant in the b direction, which differs by more than 15%. This disparity highlights the influence of NPT equilibration on the lattice constants, particularly in the b direction, and emphasizes the intrinsic mechanical properties of α-quartz. The

b direction, represented by the plane [0 1 0], corresponds to the transverse orientation with the lowest Young's modulus. As a result, during the NPT simulation, it experiences the highest stretching, making it more challenging to control compared to the a and c directions.

The radial distribution functions (RDFs) vary as the microstructural characteristics of a material change. The RDF of void-free α-quartz were determined for all atom pairs (O-O, O-Si and Si-Si) using the trajectories obtained from the three potentials. The results are compared to the experimental data in Figures 4(a)–(c). Ideally, the peaks of the RDFs should match with the dashed lines, representing the experimental values [66]. When comparing between the MD simulation results, those with peaks closer to the experimental values indicate the capability of a potential to accurately reproduce the structure of α-quartz. In Figure 4a, the RDF peaks corresponding to both BKS and Vashishta potentials are close to the experimental values, while that of the Tersoff potential is much larger than all four experimental O-O bond lengths. Similar observations are made with respect to the O-Si and Si-Si bond lengths. In general, the Tersoff potential significantly overestimates all three bond lengths for α-quartz. The RDF results obtained by the Tersoff potential are not as accurate as those obtained by the BKS and Vashishta potentials.

3.2. Mechanical behavior of α-quartz under tension

In this section, the tensile properties of void-free and single-void α-quartz, as determined from the MD simulations using the BKS, Tersoff, and Vashishta potentials are discussed. Two different ensembles, i.e., NVT (constant Number of atoms, Volume, and Temperature) and NPT (constant Number of atoms, Pressure, and Temperature), were separately applied to investigate the uniaxial strain and uniaxial stress behaviors of α-quartz. In the NVT ensemble, the volume of the simulation cell was kept fixed for each time step and the temperature was controlled, allowing the

quartz sample to deform in the *z* direction. Conversely, in the NPT ensemble, the volume of the simulation cell was allowed to change, while the pressure and temperature were controlled to maintain a constant pressure on the system while applying uniaxial stress. The use of these two ensembles enables the simulations under two different mechanical states, the uniaxial strain and uniaxial stress conditions, respectively, and thus can provide in-depth insight and understanding into the mechanical behavior of α-quartz.

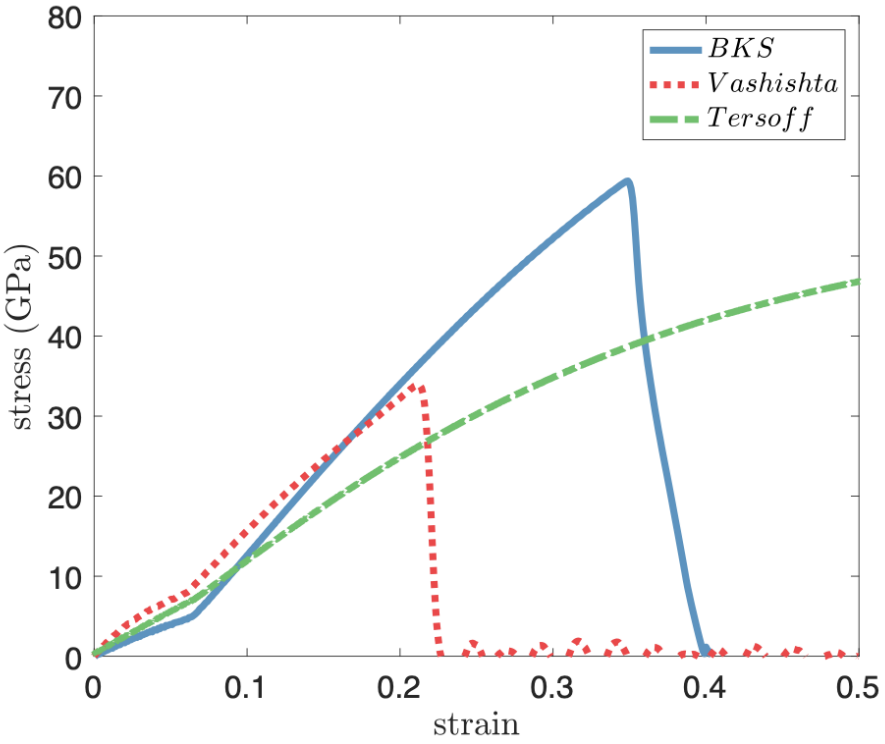

Figure 5. Stress-strain curves of void-free α-quartz in uniaxial strain condition, predicted by the BKS, Vashishta, and Tersoff potentials.

3.2.1 Tensile properties of void-free α-quartz under uniaxial strain condition

The tensile stress-strain (σ - ε) curves for void-free α-quartz under uniaxial strain condition are depicted in Figure 5. The tensile properties were obtained for the [001] direction of the quartz crystal at a constant strain rate of 0.01/ps by applying the NVT ensemble. The observation of the stress-strain curves in blue and red in Figure 5 indicates the brittle fracture behavior of α-quartz,

which is accurately captured by the BKS and Vashishta potentials, despite significant differences in ultimate tensile strength and elongation rate at fracture. The BKS potential yields an ultimate tensile strength exceeding 60 GPa, whereas the Vashishta potential produces a 43% lower value. Moreover, the simulation utilizing the BKS potential exhibits a strain of 0.35 at fracture, while Vashishta yields at the strain of 0.21. The contrasting mechanical behavior highlights the variation in deformation mechanisms between these two potentials.

As shown in Figure 5, the Tersoff potential could reproduce the elastic response of α-quartz under tension, but it does not capture the brittle behavior of α-quartz within the strain range of 0.5 studied in the present work. In the Tersoff or Tersoff-like force fields, the utilization of "soft" cut-off distances, e.g., R_1 and R_2 in Eq. (7), can introduce non-physical strain hardening effects in the uniaxial stress-strain curve. Consequently, this can lead to unrealistic predictions of material strength and strain. Similar founds have been observed when applying the Tersoff potential in MD simulations to analyze the tensile behaviors of materials [68–70]. In experimental settings, when a material is subjected to uniaxial stress, it undergoes plastic deformation, which involves the motion of dislocations. The presence of dislocations leads to strain hardening, where the material becomes stronger as it is deformed further. While the “soft” cut-off treatment used in the Tersoff and Tersoff-like force fields is computationally convenient and allows for efficient simulations, however, it can artificially enhance this strain hardening effect, thus giving rise to an overestimation of the fracture strength and strain.

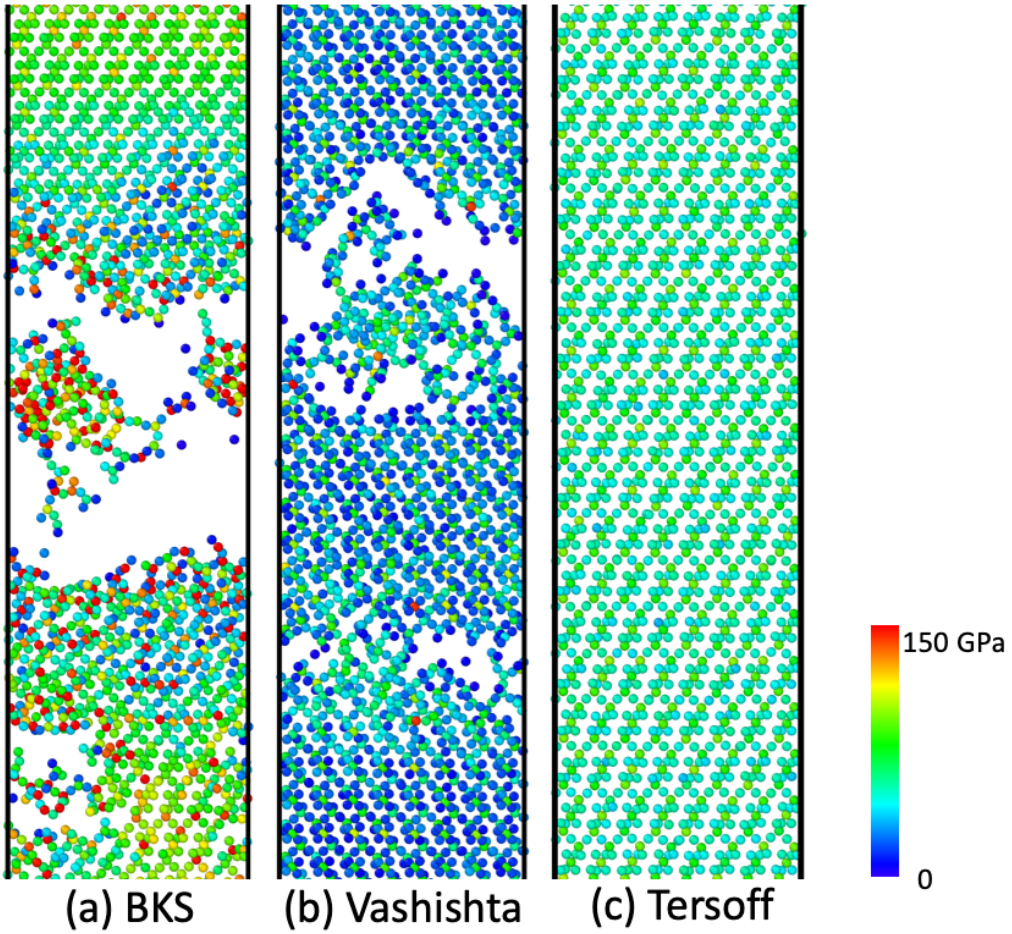

Figure 6. Atomistic equivalent stress distribution that denotes the fracture for void-free α-quartz, predicted by the (a) BKS, (b) Vashishta, and (c) Tersoff potentials. The atoms are colored according to the equivalent stress value from 0 to 150 GPa.

As mentioned previously, it is challenging for an interatomic potential to accurately capture the fracture behavior of a crystalline material system. To better understand the fracture mechanism of α-quartz under uniaxial strain condition, the fracture characteristics of the perfect single-crystal α-quartz are compared among the three potentials, as shown in Figure 6. The atomic equivalent stress distribution is described by means of the von Mises stress σ_{VM}, which is given by:

$$\sigma_{VM} = \left(\frac{1}{2}\left[\left(\sigma_{xx} - \sigma_{yy}\right)^2 + \left(\sigma_{xx} - \sigma_{zz}\right)^2 + \left(\sigma_{zz} - \sigma_{yy}\right)^2 + 6\left(\sigma_{xy}^2 + \sigma_{xz}^2 + \sigma_{yz}^2\right)\right]\right)^{1/2} \quad (10)$$

where σ_{ij} ($i = x, y, z$, and $j = x, y, z$, respectively) are the components of the atomic strain tensor. Upon the observation of Figure 6, it is apparent that both Vashishta and BKS potentials are capable to describe the brittle damage near their fracture points. The Vashishta potential yields a fracture strain (ε_f) value of 0.26, while the utilization of the BKS potential exhibits a substantial 35% increase in the strain at fracture, resulting in a value of 0.35. The Tersoff potential does not show any sign of material rupture even at a large deformation of $\varepsilon_f = 0.40$ (Figure 6c). By comparing Figure 6(a), (b) and (c), it could be noted that the utilization of the BKS potential allows for the detection of stress concentration in α-quartz. Higher equivalent stresses are generated around or close the fracture surface, indicating an uneven stress distribution within the materials. In Figure 6(b) and (c), the stress concentration is difficult to observe by using both Vashishta and Tersoff. Consequently, the use of BKS potential provides a more accurate description of the fracture behavior in α-quartz among all three potentials. Further discussion regarding fracture analysis for the α-quartz structures with different sizes of single voids will be conducted in Section 3.2.4.

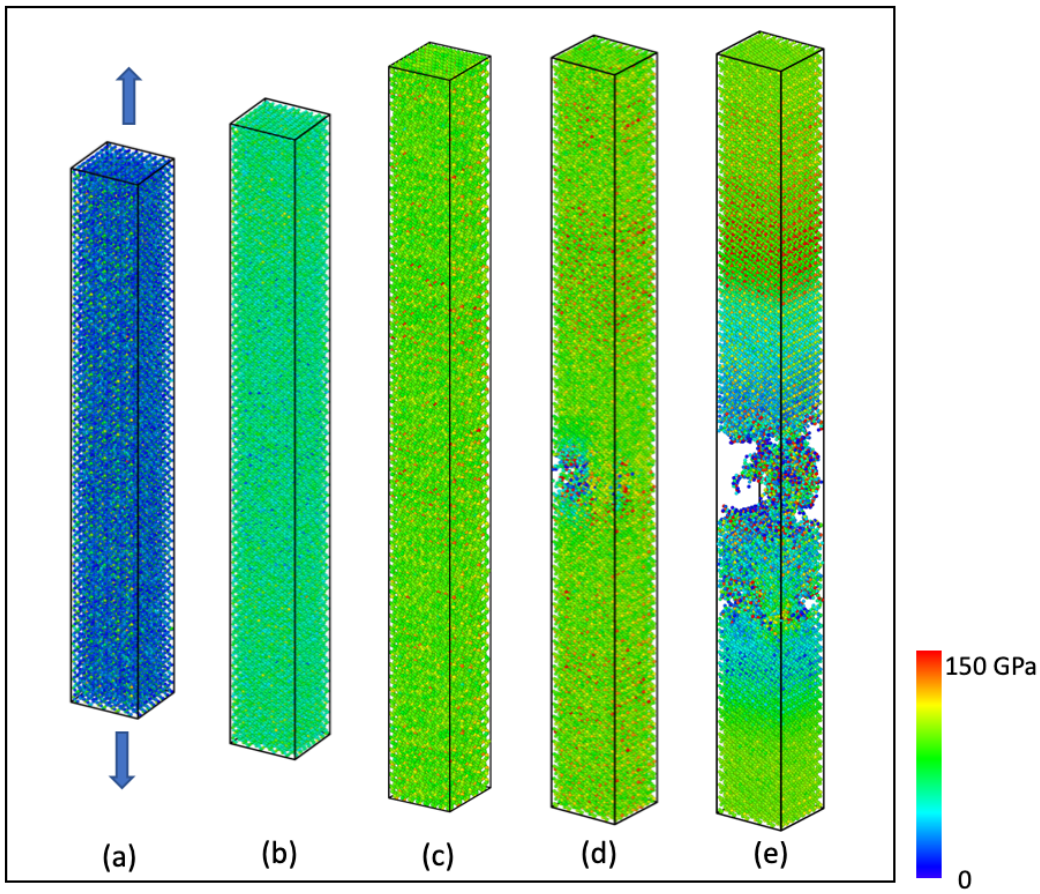

Figure 7. Deformation snapshots of the void-free α-quartz at different simulation time steps: (a) before applying tensile stress and after equilibrium, (b) before the failure point at the strain of 0.2, (c) at the beginning of the failure point (strain of 0.34), (d) in the middle of the failure (strain of 0.35) and (e) after the failure (strain of 0.36). The atoms are colored according to the equivalent stress value from 0 to 150 GPa.

Figure 7 depicts the time evolution of tensile deformation for the void-free α-quartz, predicted by the BKS potential with the NVT ensemble. The atoms colored according to the atomic equivalent stresses at different simulation time steps. At the initial stage of deformation, stress increases in the elastic region with strain, which is an expected behavior in such material. The snapshot in Figure 7(c) at a strain of 0.34 shows no cracks forming in the sample. However, Figure 7(d) and (e) demonstrate the occurrence of failure for α-quartz, with rapidly generating cracks in the middle of the sample. Figure 7(d) represents the point on the stress-strain curve where the

maximum stress before failure occurs, then immediately after the failure point, the stress is released and the breakage of the material is observed (Figure 7(e)). The short time duration of crack nucleation and growth indicates the brittle mode of failure as observed experimentally. Additionally, the presence of high equivalent stress around the cracks is noticeable in Figure 7(e). This high stress concentration is often a significant factor contributing to the propagation or growth of the cracks and can influence the overall failure behavior of the material.

3.2.2 Tensile properties of void-free α-quartz under uniaxial stress condition

To gain more insight into the mechanical response of α-quartz, an NPT ensemble was utilized in the MD simulation to perform the tensile test under uniaxial stress condition. Figure 8 displays the comparison of the stress-strain curves predicted by the BKS, Vashishta and Tersoff potentials with both NVT and NPT ensembles. It is apparent to find that the material behavior under uniaxial stress state is distinct from that under uniaxial strain state. Both BKS and Vashishta potentials exhibit notable disparities in predicting the ultimate tensile strengths and elongation rates at break. In the NPT simulation under the uniaxial stress state (Figure 8a), the utilization of the BKS potential results in a 14% decrease in the ultimate strength and a 11% decrease in the fracture strain when compared to the uniaxial stress state. Moreover, by employing the BKS potential under the NPT simulation, residual stress remains in the sample during the post-failure process, which is showing the correct mechanical response. The variation of the underlying deformation mechanisms between the two tension states could cause different mechanical responses before and after failure. When the Vashishta potential is employed, an increase of 20% in the ultimate strength and an increase of 24% in the fracture strain are observed under the uniaxial stress state. However, the Tersoff potential as shown in Figure 8c, while applied to both uniaxial

strain and stress states, fails to accurately predict the brittle fracture behavior of α-quartz. Nevertheless, a comparison of those tensile curve patterns reveals perceptible differences in their shapes. These noticeable dissimilarities for all three potentials suggest that the external loading conditions imposed on the simulated atomistic system, along with the choice of interatomic potentials, indeed influence the mechanical response of such materials.

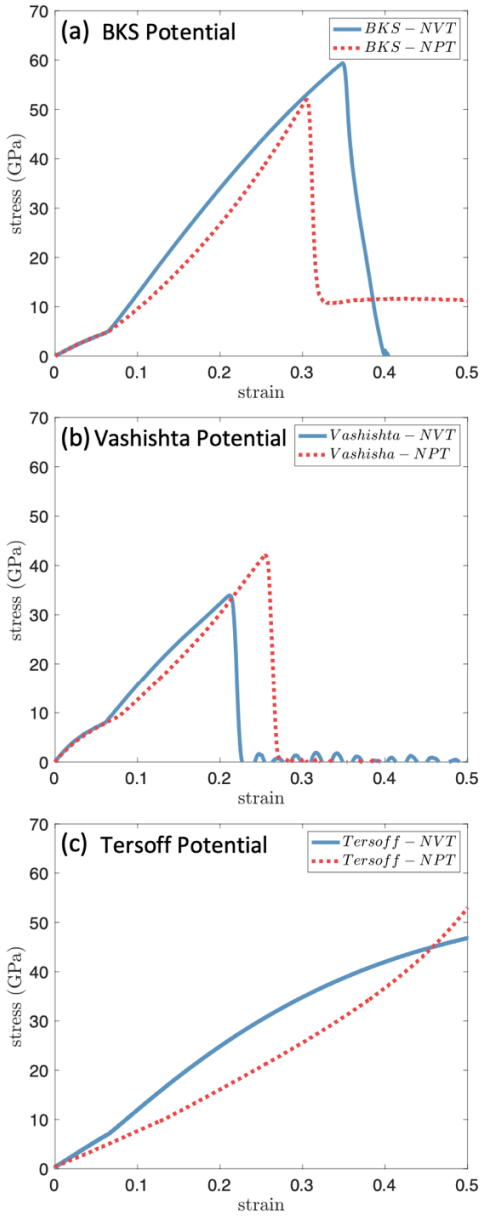

Figure 8. Comparison of the stress-strain curves of void-free α-quartz between NVT and NPT ensembles, predicted by (a) BKS, (b) Vashishta, and (c) Tersoff potentials.

Table 4. Young's moduli, ultimate strengths, and strains at fracture of α-quartz, predicted by the BKS, Vashishta, and Tersoff potentials.

	Young's Modulus (GPa)	**Ultimate Strength** (GPa)	**Strain at Fracture** (%)
BKS	99.9	51.9	0.31
Vashishta	103.7	42.1	0.25
Tersoff	73.5	--	--

To further compare all three potentials by using NPT ensemble, the values of Young's moduli, ultimate strengths, and strains at fracture are summarized in Table 4. Young's moduli were calculated using the initial linear portion of the stress-strain curves corresponding to each potential. It is worth noting that the BKS potential provides an excellent description for the elastic deformation of α-quartz. The Young's modulus of α-quartz predicted by the BKS potential is 99.9 GPa, which is in excellent agreement with the experimental value of 97.9 GPa at 298 K for crystalline α-quartz [71]. Although the fracture region appears in the stress-strain curve associated with the Vashishta potential, the value of Young's modulus (103.7 GPa) is slightly overestimated when compared to the experimental value. Based on the observation from Table 4, the Vashishta potential predicts the highest values for Young's modulus, whereas the Tersoff potential estimates the lowest. Overall, the Tersoff potential significantly underestimates the Young's modulus and fails to provide any information regarding the fracture parameters of α-quartz.

3.2.3. Tensile properties of single-void α-quartz

In this section, the mechanical behavior of crystalline α-quartz with nanovoid structures is described by utilizing NVT and NPT ensembles. For this purpose, the stress-strain curves of single-void structures are compared to that of the void-free in Figure 9. We simulated single-void α-quartz models containing two different void radii of 2.5 and 15 Å, respectively at a constant

strain rate of 0.01/ps. The presence of a void within the α-quartz structure was observed to have an impact on the tensile strength and fracture strain, regardless of the utilization of different potentials and ensembles. Figure 9a illustrates that the introduction of voids with sizes of 2.5 and 15 Å in the structure leads to a decrease in its ultimate tensile strength predicted by the BKS by 19% and 72%, respectively, by utilizing the NVT ensemble. Additionally, the strain at fracture of α-quartz decreases by 21% and 63% for void sizes of 2.5 and 15 Å, respectively. Similar results were obtained for the Vashishta potential (Figure 9b). Note that the Vashishta potential demonstrates an oscillatory or "ringing" behavior beyond the peak limit point. This phenomenon is due to the stress waves that travel back and forth, particularly with the case of α-quartz with a single void. For the Tersoff potential, when using both NVT and NPT ensembles, the stress-strain curves do not exhibit any noticeable difference upon introducing a small void with the size of 2.5 Å. However, a large void with a radius of 15 Å can significantly affect the tensile properties, especially under the uniaxial strain condition. In Figure 9(c), brittle fracture is observed in the single-void structure with the size of 15 Å, which exhibits a tensile strength of 33.6 GPa and a fracture strain of 0.33. These results indicate that structural defect in α-quartz, such as a spherical nanovoid, may significantly reduce its mechanical properties, and the extent of this reduction is highly correlated with the void size.

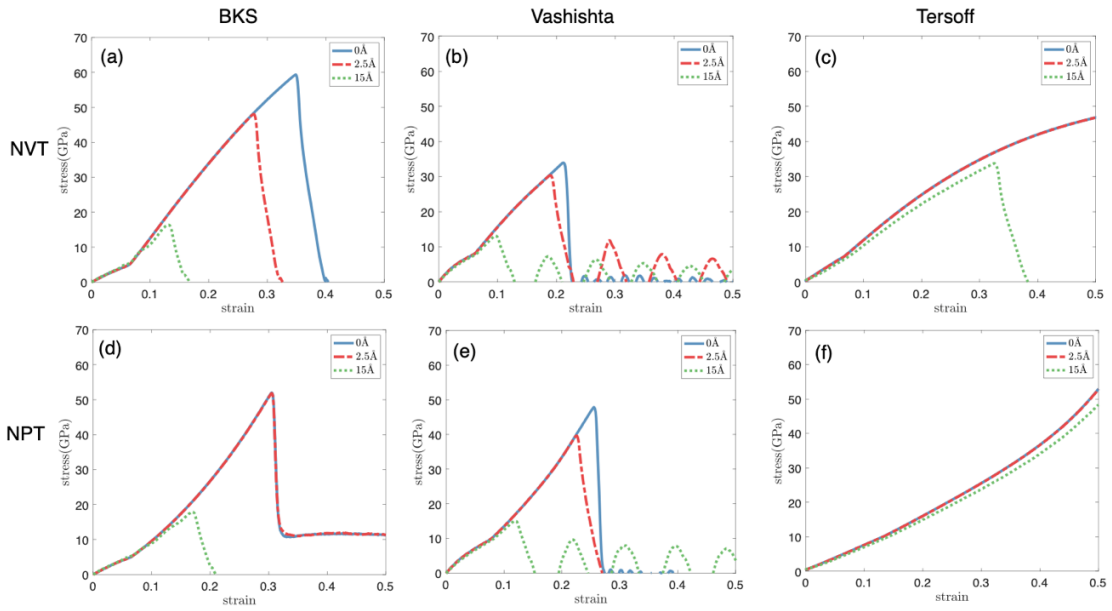

Figure 9. Tensile stress-strain curves of single-void α-quartz with different void sizes utilizing (a)-(c) NVT and (d)-(f) NPT ensembles. Simulations are predicted by (a)(d) BKS, (b)(e) Vashishta and (c)(f) Tersoff potentials.

To better understand the distinction between the NVT and NPT simulations in tension studies of α-quartz, the predicted mechanical responses of the single-void quartz structures with the two ensembles are compared in Figure 9. In the case of the small single-void model with the void size of 2.5 Å, the results obtained for the BKS potential with the two ensembles differ significantly. The presence of the small void has a notable impact on the mechanical properties of α-quartz, as predicted by NVT simulation. However, this is not the case for the NPT simulation. This observation suggests that voids may have a significant influence on the materials under uniaxial strain when the BKS potential is used. For the Vashishta potential, the small void clearly caused a reduction in the tensile properties of α-quartz, as predicted by both NVT and NPT simulations. The tensile curve patterns are quite similar in those two cases, except that slightly higher tensile properties are obtained when the NPT ensemble is used during MD simulation. Interestingly, the Tersoff potential shows no difference in the tensile curves between the void-free

quartz and the small single-void model, regardless of whether NPT or NVT ensemble is used. No brittle damage is detected in the stress-strain curves for the small single-void models (2.5 Å), as evident in both Figures 9(c) and 9(f).

With respect to the single-void α-quartz structure with the large void size of 15 Å, both the BKS and Vashishta potentials result in a dramatic reduction in the ultimate strength and elongation at fracture of α-quartz. However, when using the Tersoff potential, a fracture region appears at a strain of 0.33 in the NVT ensemble. Nevertheless, the elongation at break is too large to be comparable with experimental data or the results obtained using the other two potentials. All tensile curves obtained with the Tersoff potential exhibited very high strengths and large fracture strains, indicating the unrealistic elongation in all models that led to an overestimation of the tensile properties.

3.2.4 Fracture process of single-void α-quartz

To further investigate all three potentials and reveal the fracture mechanism of single-void α-quartz under tensile loading, snapshots of the equivalent stress distribution (structural evolution of the single-void α-quartz structures) in uniaxial strain state are illustrated in Figure 10 and 11. The equivalent stress for each atom was calculated for two single-void structures with the BKS, Vashishta, and Tersoff potentials.

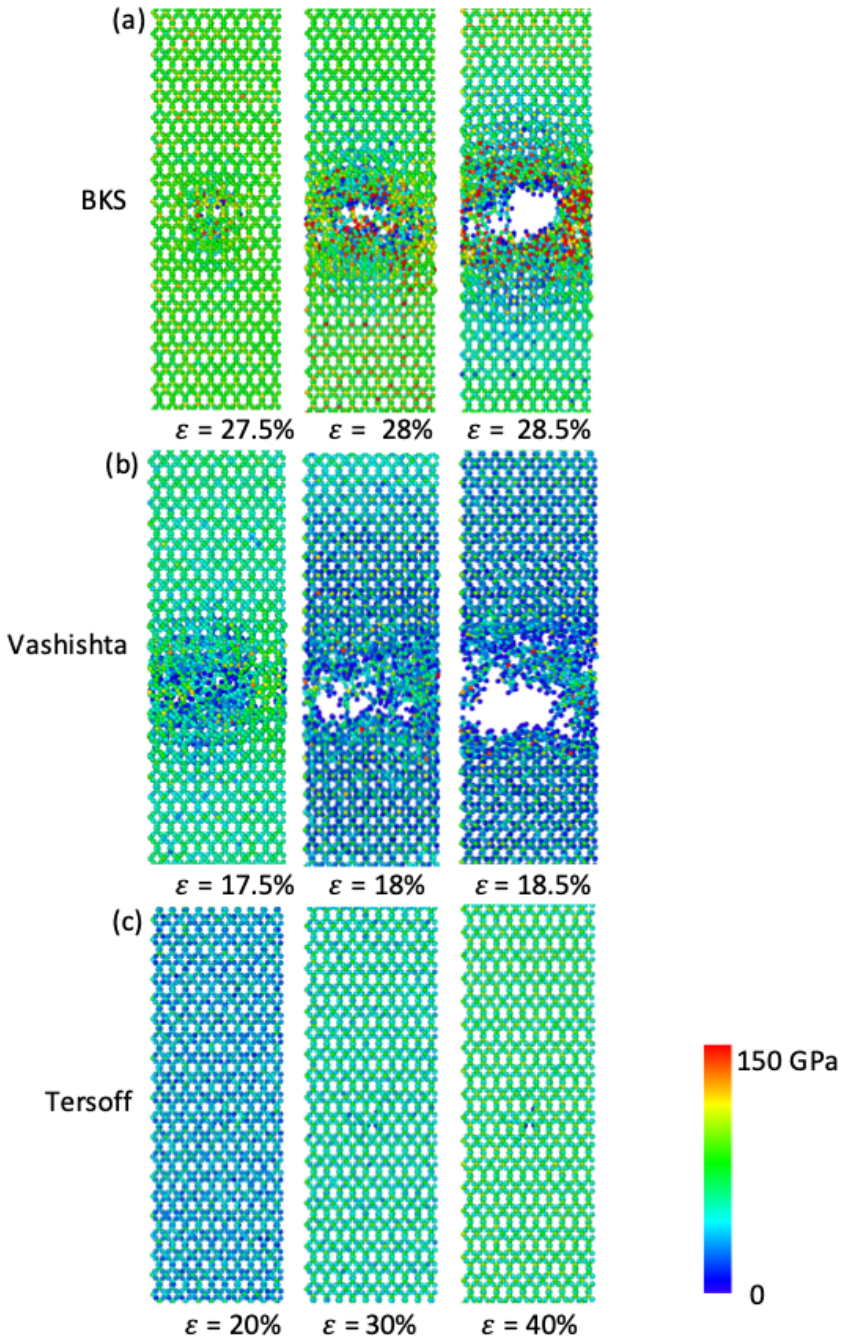

Figure 10. Atomistic views of the equivalent stress distribution in the single-void α-quartz structure with the void size of 2.5 Å before and after failure, predicted by the (a) BKS, (b) Vashishta, and (c) Tersoff potentials. Atoms are colored with the equivalent stress values. Red color indicates the highest and blue color represents the lowest stress.

The atomistic configurations with the equivalent stress distribution before and after fracture in the single-void α-quartz structure with the smaller void size of 2.5 Å are provided in Figure 10.

The models were subjected to the uniaxial strain condition by applying an NVT ensemble. The snapshots were captured before and after failure within specific elongation ranges (27.5 - 28.5% for the BKS potential and 17.5-18.5% for the Vashishta potential), as shown in Figures 10(a) and 10(b), respectively. The fracture behavior could be easily observed for both potentials with fractures occurring rapidly within a narrow elongation strain range of 1%. This indicates that such brittle materials do not undergo significant plastic deformation. The failure behavior observed in both cases is attributed to the breakage of the atomic bonds, which is facilitated by the presence of voids that lead to stress concentration. While the equivalent stress is typically associated with macroscopic distortion energy, it has been demonstrated that the movement of defects at the nanoscale plays a crucial role in the material deformation and crack growth. This suggests that the behavior of defects at the atomic level can significantly influence the macroscopic response of α-quartz. The equivalent stress distributions are illustrated for each interatomic potential around its rupture stage, highlighting the correlation between the void and stress distribution.

By direct inspection, the high equivalent stresses are observed to be concentrated around the void for the BKS potential, while the Vashishta potential exhibits much lower stress values in this region. The BKS potential shows high stress values (~150 GPa) both before and after failure near the edges of the spherical void, indicating the stress concentration around the edges of this small void. The stress tends to concentrate and become higher in magnitude around these regions compared to the surrounding material. The exact stress distribution will depend on factors such as the shape and size of the void, as well as the external applied load. It should also be noted that the stress distribution in Figure 10(a) is not perfectly uniform or symmetric, indicating the anisotropy of the α-quartz models. Conversely, the equivalent stress distribution for the Vashishta potential (Figure 10(b)) does not effectively describe the stress concentration around the void structure.

When considering the Tersoff potential (Figure 10(c)), the structure seems to be stretched quite evenly without any stress concentration throughout the investigated area. No failure phenomenon is observed at elongation ratios of 20%, 30%, or even 40%, suggesting that α-quartz behaves like a ductile material, as predicted by the Tersoff potential. This is inconsistent with the typical brittleness observed in such materials under tension. In summary, the BKS potential provides a more satisfactory description of stress concentration around the void compared to the Tersoff or Vashishta potential.

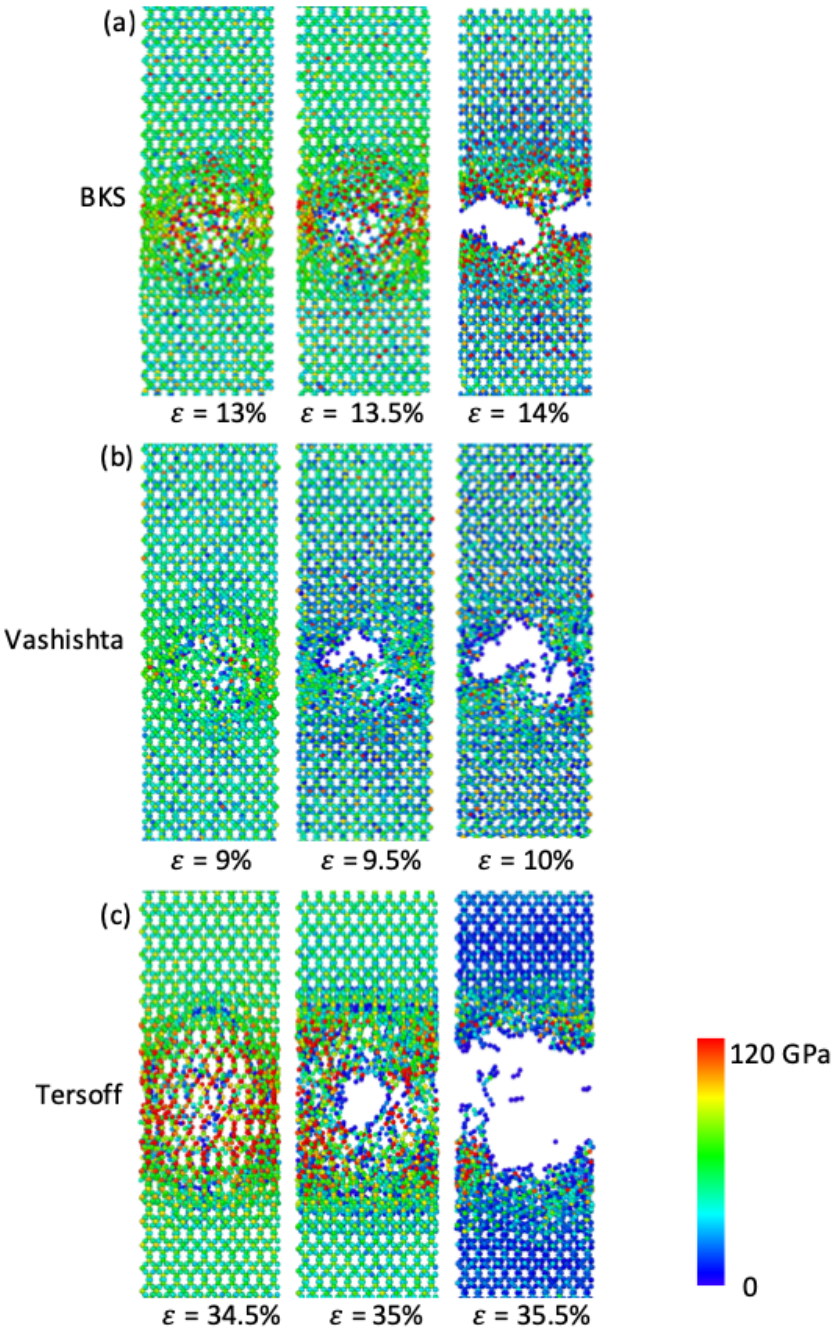

Figure 11. Atomistic views of the equivalent stress distribution in the single-void α-quartz structure with the void size of 15 Å before and after failure, predicted by the (a) BKS, (b) Vashishta, and (c) Tersoff potentials. Atoms are colored with the equivalent stress values.

As the size of the void increases, the equivalent stress distributions around the void with a size of 15 Å are shown in Figure 11 for all three potentials. Comparing the structures with large

and small void sizes in Figure 10 and 11, it is found that the presence of a large void leads to a more pronounced stress concentration around its surface, especially in the initial stage of failure. By using the BKS potential at the strain of 27.5%, local stress concentration is distinctly noticed. Hence, the specific behavior of stress concentration around the void in α-quartz is highly related to the size of the void. In Figures 11(a) and 11(b), the stress concentration is effectively described by using the BKS potential, while the presence of the void does not show any significant impact on the stress distribution, as predicted by the Vashishta potential. The Tersoff potential behaves differently for the two different single-void quartz structures shown in Figures 10(c) and 11(c). While fracture can hardly be observed for the small void structure, stress concentration does occur around the large spherical void with the radius of 15 Å. However, for the Tersoff potential, the non-physical strain hardening in the stress-strain curve results in unrealistic material strength and strain. The elongation strain is 35.5%, as predicted by the Tersoff potential, which is several times higher than that of the BKS (ε_f = 14%) and Vashishta (ε_f = 10%) potentials.

The strain rate shows a considerable influence on the calculated stress-strain responses in the uniaxial strain state predicted by the BKS potential, as observed in Figure 12. The single-void α-quartz structures with the two void sizes were investigated, and tensile loading was applied with two different strain rates of 0.01 and 0.001/ps. The findings reveal that both the ultimate tensile strength and elongation at fracture increase as the strain rate increases. This can be attributed to the impact of strain rate on relaxation time during tension. During each time interval of simulation, the rearrangement of atoms, bonds, and angles reach local equilibria (stress release) after deformation. A lower strain rate results in a longer relaxation time and leads to a more extensive equilibrium process for the entire system, especially at the highest unstable state of deformation

just before failure. This leads to a lower material strength. It should be noted that Young's modulus remains unaffected by the strain rate, as depicted in Figure 12.

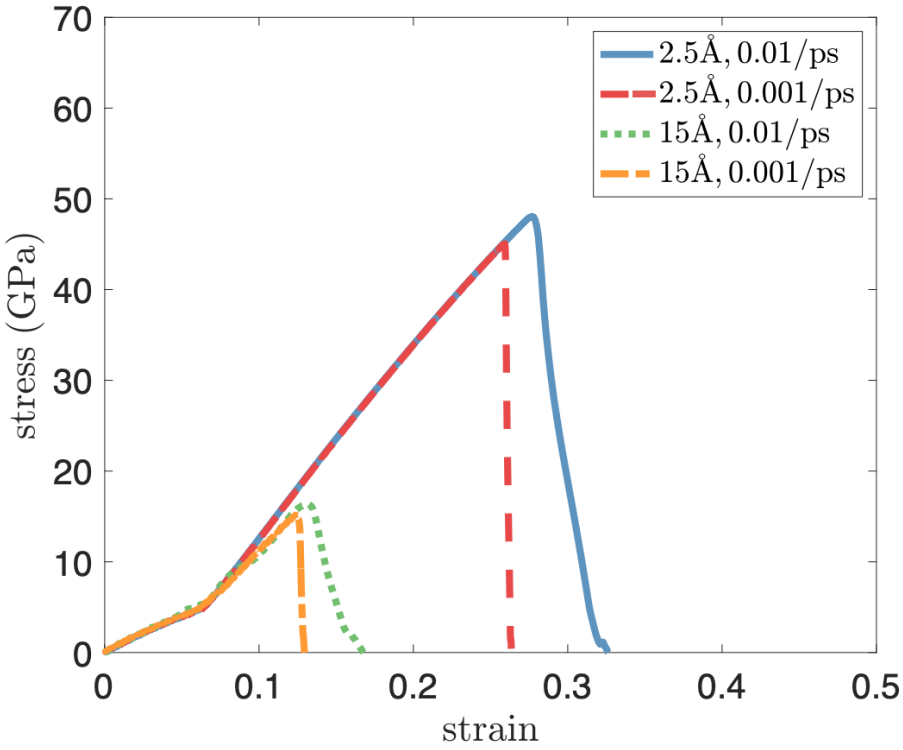

Figure 12. Tensile stress-strain curves for the single-void α-quartz structures with two void sizes of 2.5 and 15 Å obtained at strain rates of 0.01 and 0.001/ps, as predicted by the BKS potential.

CHAPTER 5

CONCLUSIONS

In this work, molecular dynamics simulation was employed to study the structural and mechanical properties of void-free and single-void α-quartz structures. Three interatomic potentials, i.e., BKS, Vashishta, and Tersoff, were utilized in the simulations to simulate the tension and fracture behavior of three α-quartz structures. Two distinct ensembles, NVT and NPT, were employed in tensile tests to simulate two different mechanical states, i.e., uniaxial strain and uniaxial stress, respectively. The main findings of the work are summarized below:

- The BKS and Vashishta potentials provide accurate predictions of the equilibrium structures of perfect single-crystal α-quartz. The BKS potential yields a density of 2.662 g/cm3, which closely agrees with the reported value of 2.60 g/cm3. In contrast, the Vashishta potential suggests a slightly lower density of 2.511 g/cm3. However, the Tersoff potential significantly underestimates the density of α-quartz. When examining the lattice constants, the Vashishta and BKS potentials exhibit good agreement with experimental values, differing by approximately 3% and 5% respectively. Conversely, the Tersoff potential deviates considerably from experimental values, particularly in the lattice constant along the b direction, which differs by over 15%. By analyzing the RDF, it is evident that the BKS and Vashishta potentials offer favorable predictions for the α-quartz structures. In contrast, the Tersoff potential consistently overestimates all three bond lengths.
- For a void-free α-quartz crystal, the BKS potential provides an accurate depiction of its tensile properties by successfully predicting stress-strain curves. Similarly, the Vashishta potential can capture the fracture behavior in void-free α-quartz, although it exhibits some tendency to over-predict Young's modulus under uniaxial stress conditions. The Tersoff potential effectively captures the elastic region of the stress-strain curve but falls short in accurately predicting the fracture behavior of void-free α-quartz.

- In the context of single-void α-quartz structures, the presence of a spherical defect can have a significant detrimental effect on the mechanical properties, with the degree of reduction being closely linked to the void size. Utilizing the BKS potential, the introduction of voids measuring 2.5 and 15 Å in the structure results in a notable decrease in ultimate tensile strength by 19% and 72% respectively when using the NVT ensemble. Moreover, the strains at fracture also experience reductions of 21% and 63% respectively. These findings are consistent with the outcomes obtained using the Vashishta potential. Conversely, when employing the Tersoff potential with both the NVT and NPT ensembles, the stress-strain curves do not exhibit any discernible differences upon introducing a smaller void with a size of 2.5 Å.
- The choice of ensembles, such as NVT or NPT, plays a significant role in influencing the mechanical response of α-quartz, due to the difference between uniaxial strain problem and uniaxial stress problem. When utilizing the BKS potential, the presence of a smaller void with a radius of 2.5 Å has a notable impact on the tensile properties of the material in the NVT simulation, whereas there is no significant influence observed in the NPT simulation. With the Vashishta potential, the patterns of the tensile curves are quite similar in both NVT and NPT simulations, albeit slightly higher tensile properties can be obtained when using the NPT ensemble. In the case of the Tersoff potential, brittle fracture occurs at a strain of 0.33 in the NVT ensemble, while it is not observed in the NPT ensemble. However, the tensile strength and elongation at break for the Tersoff potential are excessively large compared to the results obtained using the other two potentials. This discrepancy can be attributed to the "soft" cut-off treatment in the Tersoff potential, which leads to non-physical strain hardening in the stress-strain curve, thereby resulting in an overestimation of the material strength and strain.

- Examinations of the equivalent stress distributions for α-quartz structures reveal their microscopic fracture mechanisms under uniaxial strain state. BKS potential can better describe the stress concentration around both voids with the radii of 2.5 Å and 15 Å, while the presence of the voids does not show any significant impact on such stress distribution by Vashishta. It is noteworthy that the Tersoff potential behaves differently for two different single-void structures. While the fracture can hardly be observed for the smaller void structure, stress concentration does occur around the larger spherical void with 15 Å along with an unrealistic large elongation for α-quartz.

It is essential to emphasize that the interatomic potentials discussed in this context are empirical models derived from approximations of true atomic interactions, which inherently impose limitations. When investigating material properties, it is always prudent to carefully consider the strengths and weaknesses of these potentials and validate their predictions against experimental data whenever feasible. By doing so, one can ensure a more reliable and accurate understanding of the materials under study. The results and discussions in this work are intended to offer some guidance for atomistic modeling and simulation of silica materials by aiding in the selection of appropriate atomic potentials. However, it is crucial to recognize that further validation and refinement through experimental validation is necessary to enhance the applicability of making informed decisions and advancing the understanding of silica materials through atomistic modeling and simulation.

BIBLIOGRAPHY

1. Battey, M. H. *Mineralogy for students*. (Longman, 1979).
2. Wenk, H.-R. & Bulakh, A. G. *Minerals: their constitution and origin*. (Cambridge University Press, 2004).
3. Klein, C. *Solutions manual to accompany Minerals and rocks: exercises in crystallography, mineralogy, and hand specimen petrology*. (Wiley, 1990).
4. Hazen, R. M., Finger, L. W., Hemley, R. J. & Mao, H. K. High-pressure crystal chemistry and amorphization of α-quartz. *Solid State Communications* **72**, 507–511 (1989).
5. Molaei, F. & Siavoshi, H. Molecular dynamics studies of thermal conductivity and mechanical properties of single crystalline α-quartz. *Solid State Communications* **320**, 114020 (2020).
6. Ghashoghchi, R. A., Hosseini, M. R. & Ahmadi, A. Effects of microbial cells and their associated extracellular polymeric substances on the bio-flocculation of kaolin and quartz. *Applied Clay Science* **138**, 81–88 (2017).
7. Li, W. L., Lu, K. & Walz, J. Y. Freeze casting of porous materials: review of critical factors in microstructure evolution. *International Materials Reviews* **57**, 37–60 (2012).
8. Kresge, C. T., Leonowicz, M. E., Roth, W. J., Vartuli, J. C. & Beck, J. S. Ordered mesoporous molecular sieves synthesized by a liquid-crystal template mechanism. *Nature* **359**, 710–712 (1992).
9. Beck, J. S. *et al.* A new family of mesoporous molecular sieves prepared with liquid crystal templates. *J. Am. Chem. Soc.* **114**, 10834–10843 (1992).
10. Zhao, D., Huo, Q., Feng, J., Chmelka, B. F. & Stucky, G. D. Nonionic Triblock and Star Diblock Copolymer and Oligomeric Surfactant Syntheses of Highly Ordered,

Hydrothermally Stable, Mesoporous Silica Structures. *J. Am. Chem. Soc.* **120**, 6024–6036 (1998).

11. Ryoo, R., Kim, J. M., Ko, C. H. & Shin, C. H. Disordered Molecular Sieve with Branched Mesoporous Channel Network. *J. Phys. Chem.* **100**, 17718–17721 (1996).
12. Bagshaw, S. A., Prouzet, E. & Pinnavaia, T. J. Templating of Mesoporous Molecular Sieves by Nonionic Polyethylene Oxide Surfactants. *Science* **269**, 1242–1244 (1995).
13. Walcarius, A. Mesoporous materials and electrochemistry. *Chem. Soc. Rev.* **42**, 4098 (2013).
14. Linares, N., Silvestre-Albero, A. M., Serrano, E., Silvestre-Albero, J. & García-Martínez, J. Mesoporous materials for clean energy technologies. *Chem. Soc. Rev.* **43**, 7681–7717 (2014).
15. Ye, Y., Jo, C., Jeong, I. & Lee, J. Functional mesoporous materials for energy applications: solar cells, fuel cells, and batteries. *Nanoscale* **5**, 4584 (2013).
16. Vekariya, R. L., Dhar, A., Paul, P. K. & Roy, S. An overview of engineered porous material for energy applications: a mini-review. *Ionics* **24**, 1–17 (2018).
17. Yuan, L., Ding, S. & Wen, C. Additive manufacturing technology for porous metal implant applications and triple minimal surface structures: A review. *Bioactive Materials* **4**, 56–70 (2019).
18. Cho, H., Bartl, M. H. & Deo, M. Bubble Point Measurements of Hydrocarbon Mixtures in Mesoporous Media. *Energy Fuels* **31**, 3436–3444 (2017).
19. Rashidi, S., Esfahani, J. A. & Rashidi, A. A review on the applications of porous materials in solar energy systems. *Renewable and Sustainable Energy Reviews* **73**, 1198–1210 (2017).
20. *Industrial and Technological Applications of Transport in Porous Materials*. vol. 36 (Springer Berlin Heidelberg, 2013).

21. Domingos, R., Tremblay, M. M., Shuster, D. L. & Militzer, B. Simulations and Experiments Reveal Effect of Nanopores on Helium Diffusion in Quartz. *ACS Earth Space Chem.* **4**, 1906–1912 (2020).
22. Lasaga, A. C. & Gibbs, G. V. Applications of quantum mechanical potential surfaces to mineral physics calculations. *Phys Chem Minerals* **14**, 107–117 (1987).
23. Alder, B. J. & Wainwright, T. E. Studies in Molecular Dynamics. I. General Method. *The Journal of Chemical Physics* **31**, 459–466 (1959).
24. Alder, B. J. & Wainwright, T. E. Phase Transition for a Hard Sphere System. *The Journal of Chemical Physics* **27**, 1208–1209 (1957).
25. Rahman, A. Correlations in the Motion of Atoms in Liquid Argon. *Phys. Rev.* **136**, A405–A411 (1964).
26. Wang, J., Rajendran, A. M. & Dongare, A. M. Atomic scale modeling of shock response of fused silica and α-quartz. *J Mater Sci* **50**, 8128–8141 (2015).
27. Tsuneyuki, S., Tsukada, M., Aoki, H. & Matsui, Y. First-Principles Interatomic Potential of Silica Applied to Molecular Dynamics. *Phys. Rev. Lett.* **61**, 869–872 (1988).
28. Chowdhury, S. C., Haque, B. Z. (Gama) & Gillespie, J. W. Molecular dynamics simulations of the structure and mechanical properties of silica glass using ReaxFF. *J Mater Sci* **51**, 10139–10159 (2016).
29. Yasukawa, A. Using An Extended Tersoff Interatomic Potential to Analyze The Static-Fatigue Strength of SiO₂ under Atmospheric Influence. *JSME international journal. Ser. A, Mechanics and material engineering* **39**, 313–320 (1996).

30. Carré, A., Horbach, J., Ispas, S. & Kob, W. New fitting scheme to obtain effective potential from Car-Parrinello molecular-dynamics simulations: Application to silica. *Europhys. Lett.* **82**, 17001 (2008).
31. Demiralp, E., Çağin, T. & Goddard, W. A. Morse Stretch Potential Charge Equilibrium Force Field for Ceramics: Application to the Quartz-Stishovite Phase Transition and to Silica Glass. *Phys. Rev. Lett.* **82**, 1708–1711 (1999).
32. van Beest, B. W. H., Kramer, G. J. & van Santen, R. A. Force fields for silicas and aluminophosphates based on *ab initio* calculations. *Phys. Rev. Lett.* **64**, 1955–1958 (1990).
33. Tu, Y. & Tersoff, J. Structure and Energetics of the Si- SiO 2 Interface. *Phys. Rev. Lett.* **84**, 4393–4396 (2000).
34. Pedone, A., Malavasi, G., Menziani, M. C., Cormack, A. N. & Segre, U. A New Self-Consistent Empirical Interatomic Potential Model for Oxides, Silicates, and Silica-Based Glasses. *J. Phys. Chem. B* **110**, 11780–11795 (2006).
35. van Duin, A. C. T. *et al.* ReaxFF $_{SiO}$ Reactive Force Field for Silicon and Silicon Oxide Systems. *J. Phys. Chem. A* **107**, 3803–3811 (2003).
36. Tangney, P. & Scandolo, S. An *ab initio* parametrized interatomic force field for silica. *The Journal of Chemical Physics* **117**, 8898–8904 (2002).
37. Molaei, F. Understanding the Anisotropic Mechanical Behavior of Single-Crystalline Alpha Quartz From the Insight of Molecular Dynamics. *JGR Solid Earth* **127**, (2022).
38. Shinde, P. S. *et al.* A Brief Overview of Recent Progress in Porous Silica as Catalyst Supports. *J. Compos. Sci.* **5**, 75 (2021).
39. Carretero-Genevrier, A. *et al.* Soft-Chemistry–Based Routes to Epitaxial α-Quartz Thin Films with Tunable Textures. *Science* **340**, 827–831 (2013).

40. Unger, K. K. *Porous silica, its properties and use as support in column liquid chromatography*. (Elsevier Scientific Pub. Co. ; distributors for the U.S.A. and Canada, Elsevier/North-Holland, 1979).
41. Alder, B. J. & Wainwright, T. E. Studies in Molecular Dynamics. II. Behavior of a Small Number of Elastic Spheres. *The Journal of Chemical Physics* **33**, 1439–1451 (1960).
42. Hoover, W. G., Hoover, C. G., Stowers, I. F. & Siekhaus, W. J. Interface Tribology *Via* Nonequilibrium Molecular Dynamics. *MRS Proc.* **140**, 119 (1988).
43. Hoover, W. G. *et al.* Large-scale elastic-plastic indentation simulations via nonequilibrium molecular dynamics. *Phys. Rev. A* **42**, 5844–5853 (1990).
44. Landman, U., Luedtke, W. D., Burnham, N. A. & Colton, R. J. Atomistic Mechanisms and Dynamics of Adhesion, Nanoindentation, and Fracture. *Science* **248**, 454–461 (1990).
45. Landman, U., Barnett, R.N. & Luedtke, W.D. Simulations of materials: from electrons to friction. *Phil. Trans. R. Soc. Lond. A* **341**, 337–350 (1992).
46. Kim, D. E. & Suh, N. P. Molecular Dynamics Investigation of Two-Dimensional Atomic-Scale Friction. *Journal of Tribology* **116**, 225–231 (1994).
47. Levine, R. D., Bernstein, R. B. & Levine, R. D. *Molecular reaction dynamics and chemical reactivity*. (Oxford University Press, 1987).
48. Allen, M. P. & Tildesley, D. J. *Computer simulation of liquids*. (Clarendon press, 1994).
49. Plimpton, S. Fast Parallel Algorithms for Short-Range Molecular Dynamics. *Journal of Computational Physics* **117**, 1–19 (1995).
50. Herzbach, D. Comparison of model potentials for molecular dynamics simulation of crystalline silica. (2004).

51. Dollase, W. A. Reinvestigation of the structure of low cristobalite. *Zeitschrift für Kristallographie* **121**, 369–377 (1965).

52. Kavner, A. & Duffy, T. S. Pressure–volume–temperature paths in the laser-heated diamond anvil cell. *J. Appl. Phys.* **89**, 1907 (2001).

53. Hill, R. J., Newton, M. D. & Gibbs, G. V. A crystal chemical study of stishovite. *Journal of Solid State Chemistry* **47**, 185–200 (1983).

54. Tse, J. S. & Klug, D. D. The structure and dynamics of silica polymorphs using a two-body effective potential model. *The Journal of Chemical Physics* **95**, 9176–9185 (1991).

55. Nakano, A., Kalia, R. K. & Vashishta, P. First sharp diffraction peak and intermediate-range order in amorphous silica: finite-size effects in molecular dynamics simulations. *Journal of Non-Crystalline Solids* **171**, 157–163 (1994).

56. Vashishta, P., Kalia, R. K., Rino, J. P. & Ebbsjö, I. Interaction potential for SiO 2 : A molecular-dynamics study of structural correlations. *Phys. Rev. B* **41**, 12197–12209 (1990).

57. Vashishta, P., Kalia, R. K., Nakano, A. & Rino, J. P. Interaction potential for silicon carbide: A molecular dynamics study of elastic constants and vibrational density of states for crystalline and amorphous silicon carbide. *Journal of Applied Physics* **101**, 103515 (2007).

58. Susman, S. *et al.* Intermediate-range order in permanently densified vitreous SiO 2 : A neutron-diffraction and molecular-dynamics study. *Phys. Rev. B* **43**, 1194–1197 (1991).

59. Vashishta, P., Kalia, R. K., Nakano, A. & Rino, J. P. Interaction potential for silicon carbide: A molecular dynamics study of elastic constants and vibrational density of states for crystalline and amorphous silicon carbide. *Journal of Applied Physics* **101**, 103515 (2007).

60. Tersoff, J. Modeling solid-state chemistry: Interatomic potentials for multicomponent systems. *Phys. Rev. B* **39**, 5566–5568 (1989).

61. Munetoh, S., Motooka, T., Moriguchi, K. & Shintani, A. Interatomic potential for Si–O systems using Tersoff parameterization. *Computational Materials Science* **39**, 334–339 (2007).

62. Tersoff, J. New empirical approach for the structure and energy of covalent systems. *Phys. Rev. B* **37**, 6991–7000 (1988).

63. Zhang, H., Shukla, M. K., Larson, S., Rajendran, A. M. & Jiang, S. Molecular dynamics study of anisotropic shock responses in oriented α-quartz single crystal. *J Mater Sci* **57**, 6688–6705 (2022).

64. Kroonblawd, M. P., Mathew, N., Jiang, S. & Sewell, T. D. A generalized crystal-cutting method for modeling arbitrarily oriented crystals in 3D periodic simulation cells with applications to crystal–crystal interfaces. *Computer Physics Communications* **207**, 232–242 (2016).

65. Cowen, B. J. & El-Genk, M. S. On force fields for molecular dynamics simulations of crystalline silica. *Computational Materials Science* **107**, 88–101 (2015).

66. Levien, L., Prewitt, C. & Weidner D. Structure and elastic properties of quartz at pressure. *American Mineralogist* **65**, 920–930.

67. Schaible, M. Empirical Molecular Dynamics Modeling of Silicon and Silicon Dioxide: A Review. *Critical Reviews in Solid State and Materials Sciences* **24**, 265–323 (1999).

68. Eshkalak, K. E., Sadeghzadeh, S. & Jalaly, M. Mechanical properties of defective hybrid graphene-boron nitride nanosheets: A molecular dynamics study. *Computational Materials Science* **149**, 170–181 (2018).

69. Zhang, Y.Y., Pei, Q.X., Sha, Z.D. & Zhang, Y.W. A molecular dynamics study of the mechanical properties of h-BCN monolayer using a modified Tersoff interatomic potential. *Physics Letters A* **383**, 2821–2827 (2019).
70. Qi-lin, X., Zhen-huan, L. & Xiao-geng, T. The defect-induced fracture behaviors of hexagonal boron-nitride monolayer nanosheets under uniaxial tension. *J. Phys. D: Appl. Phys.* **48**, 375502 (2015).
71. Pabst, W., Gregorova, E. Elastic properties of silica polymorphs-a review. **57**, 167–184 (2013).

VITA

Yu Jia received her bachelor's degree in civil engineering from Hefei University of Technology in 2007. Her graduate research focuses on theoretical modeling and molecular dynamics simulations of α-quartz and silver nanowires.